**Nilabh K. Roy**
Department of Mechanical Engineering,
The University of Texas at Austin,
204 E. Dean Keeton ETC 4.164,
Austin, TX 78712
e-mail: nilabh.roy@utexas.edu

**Obehi G. Dibua**
Department of Mechanical Engineering,
The University of Texas at Austin,
204 E. Dean Keeton ETC 4.164,
Austin, TX 78712
e-mail: ogodibua@utexas.edu

**William Jou**
Department of Mechanical Engineering,
The University of Texas at Austin,
204 E. Dean Keeton ETC 4.164,
Austin, TX 78712
e-mail: williamjou@utexas.edu

**Feng He**
Department of Mechanical Engineering,
The University of Texas at Austin,
204 E. Dean Keeton ETC 7.150,
Austin, TX 78712
e-mail: feng.he@utexas.edu

**Jihoon Jeong**
Department of Mechanical Engineering,
The University of Texas at Austin,
204 E. Dean Keeton ETC 7.150,
Austin, TX 78712
e-mail: jihoonjeong@utexas.edu

**Yaguo Wang**
Department of Mechanical Engineering,
The University of Texas at Austin,
204 E. Dean Keeton ETC 7.150,
Austin, TX 78712
e-mail: yaguo.wang@austin.utexas.edu

**Michael A. Cullinan**
Department of Mechanical Engineering,
The University of Texas at Austin,
204 E. Dean Keeton ETC 4.154,
Austin, TX 78712
e-mail: michael.cullinan@austin.utexas.edu

# A Comprehensive Study of the Sintering of Copper Nanoparticles Using Femtosecond, Nanosecond, and Continuous Wave Lasers

*A high electrical and thermal conductivity coupled with low costs make copper (Cu) an enticing alternative to aluminum for the fabrication of interconnects in packaging applications. To tap into the benefits of the ever-reducing size of transistors, it is required to increase the input/output pin count on electronic chips, and thus, minimize the size of chip to board interconnects. Laser sintering of Cu nanoparticle (NP) inks can serve as a promising process for developing these micron sized, 3D interconnect structures. However, the exact processing windows for Cu NP sintering are not well known. Therefore, this paper presents an extensive experimental investigation of the sintering processing window with different lasers including femtosecond (fs), nanosecond (ns), and continuous-wave (CW) lasers. The dependence of the processing window on Cu layer thicknesses and laser exposure durations has also been investigated. A simplified model to estimate optimum laser sintering windows for Cu NPs using pulsed lasers is presented and the predicted estimates are compared against the experimental results. Given the simplicity of the model, it is shown to provide good estimates for fluence required for the onset of sintering and the processing window for good sintering of Cu NPs.*
[DOI: 10.1115/1.4038455]

## Introduction

Semiconductor industry has followed Moore's law to facilitate reduction in transistor size by a factor of 1000× since the 1970s [1]. However, there is a large disconnect between the feature size capabilities of back end of line wafer fabrication processes and the minimum size of the chip to board interconnect structures. The multistep procedure of conventional fabrication processes leads to high complexity and high costs as well as the release of toxic waste from manufacturing [2]. Additionally, the minimum feature sizes on traditional processes are restricted based on the artifacts of the process, like maximum aspect ratio in the electroplating process. As such, additive manufacturing (AM) has risen as a viable alternative to fabricating smaller features with lower process complexity and lower cost [3,4]. Unfortunately, current commercially available metal additive manufacturing processes either have difficulty in producing true three-dimensional (3D) structures (electrohydrodynamic jet printing and direct ink writing), work only in polymers (two-photon lithography and interference lithography), or are to slow to be used in high volume manufacturing processes (electrochemical deposition) which makes them incompatible with the electronics packaging application [5]. Recently, the sintering of nanoparticles (NPs) has attracted much interest as an alternative to conventional integrated circuit fabrication techniques [2,5,6]. To bridge the gap between the process capabilities, a new AM technique called microscale selective laser sintering ($\mu$-SLS) has been developed [7–9].

One of the functional requirements for the $\mu$-SLS system is to be able to produce three-dimensional parts with 1 $\mu$m feature size. To achieve the 1 $\mu$m feature size as envisioned in the $\mu$-SLS

Contributed by the Manufacturing Engineering Division of ASME for publication in the Journal of Micro- and Nano-Manufacturing. Manuscript received June 15, 2017; final manuscript received September 6, 2017; published online December 14, 2017. Assoc. Editor: Yayue Pan.

  

system, Cu NPs are used in order to ensure that the sintered particles are at least one order of magnitude smaller than the final sintered part. Inks are used to avoid the agglomeration problems which are common with NP powders. A number of studies have been undertaken on metal NP sintering; however, the processing window for good sintering as a function of laser power, exposure time, layer thickness, and substrate is still lacking [10].

The most common materials studied for electronics additive manufacturing are silver (Ag) and gold (Au) NPs due to the stability of these materials [3,11,12]. However, the high cost tends to be a drawback in extending them to wide use in large scale applications. Other studies have been done on comparing the sintering of Au NPs on glass against that on a Cu coated substrate [13]. That study showed much higher power requirements for the metal substrate than for glass. One study was focused on continuous wave (CW) laser sintering of Cu NPs on glass substrate [14] for two-dimensional nanopatterning. However, it was limited in its scope with regard to the variation of sintering irradiance with substrate diffusivity and thickness of the Cu layer.

In order to create very small features, short pulsed lasers are commonly used because they can have a smaller heat-affected zone from pulsed lasers which reduces the damage to the substrate and minimizes the area on the substrate that gets sintered by the laser [15]. For this reason, the sintering of NPs with ns and fs lasers has been studied extensively [6,16]. Studies have been done to categorize the ablation threshold for Cu NPs using fs lasers [17,18] and to compare the results of CW sintering to pulsed laser sintering using a single substrate but with silver NPs [19] but none of these studies present processing windows that could be used to additively manufacture good parts for electronics applications. Most studies either focus on the pulsed laser sintering or ablation of nanoparticles under the same conditions, or on the sintering of Cu NPs at a few power spots or time intervals. There is limited work out on the compilation of different sintering techniques on Cu NPs. In addition, there has been very little work on testing the variation of sintering fluence/irradiance requirements with different substrates or different thicknesses of NP layers. In chip packaging, due to the variety of substrates being used (alumina, silica, silicon nitride, polyimide, etc.), the substrate can have significantly different thermal properties in different areas which makes it difficult to be able to predict beforehand the sintering fluence/irradiance required. Thus, it is required to get a thorough understanding of the dependence of sintering processing parameters for substrates with a wide range of thermal properties.

A major thermal property of the substrate that dictates the sintering fluence/irradiance is the thermal diffusivity of the substrate. It is a measure of the ratio of heat propagation and volumetric heat absorption in a material. A higher thermal diffusivity means a higher heat conduction through the material compared to the heat absorbed into the material which causes raise in the temperature of the material. This study provides a comprehensive exploration of the feasible sintering regime for Cu NPs on a variety of substrates. The experiments have been conducted on two substrates with significantly different thermal diffusivities—aluminum (thermal diffusivity—97 $mm^2/s$ [20]) and glass (0.34 $mm^2/s$ [21])—to identify the variations in the processing window with respect to the substrate's thermal diffusivity. This range of thermal diffusivity encompasses thermal diffusivities of commonly used substrates in electronic chip packaging such as alumina (12 $mm^2/s$) and silicon nitride (0.86 $mm^2/s$).

In addition to studying the effect of the thermal diffusivity of the substrate, the results from using different types of lasers, fs and ns pulsed lasers and continuous wave lasers, are also investigated in this study. Additionally, the effects of changing the power of the laser as well as changing the sintering exposure time are considered. The experiments are conducted at three different thicknesses of Cu layers, and comparing all these data, the processing window has been divided into different regions including no sintering, weak sintering, good sintering, and ablation/melting.

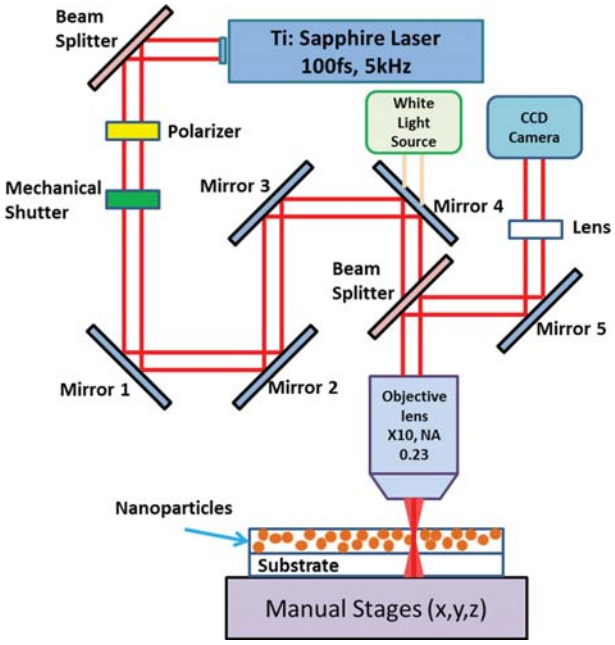


**Fig. 1 Schematic of the FS laser sintering setup**

The results of this investigation are presented in the Sintering Results section of the paper.

## Experimental Setup

**Femtosecond Laser Setup.** A Cu NP ink (CI005-G from Intrinsiq Materials, Inc., Rochester, NY) with an average particle size of 100 nm was used for this study. The NP dispersed film was prepared by spin-coating the NP ink onto the substrate (either glass or aluminum) using an EZ 6 Spin coater (Best Tools, LLC, St. Louis, MO). The obtained film was dried by hot plate heating at 85 °C for 10 min using a Corning PC-620D hot plate. The film was then irradiated by a fs laser (Spitfire ACE, Spectra Physics, Santa Clara, CA) in air with a central wavelength ($k$) of 800 nm, a repetition rate of 5 kHz, and a pulse duration of 100 fs (at FWHM). The spatial profile of the laser beam was essentially Gaussian with a beam diameter measuring 10 mm (at $1/e^2$). The laser beam passed through a shutter and a series of reflective mirrors, entered a long working distance objective lens (10×, numerical aperture NA 0.23, Mitutoyo), and focused on the Cu NP-dispersed film mounted on an $X$–$Y$ axis stage. A beam splitter and polarizer were used for controlling the intensity of the laser beam. In addition, a charge-coupled device camera and a white light source were also installed for focusing the beam, determining focal spot size, and monitoring the sintering (see Fig. 1).

**Nanosecond Laser Setup.** For the ns laser, a 532 nm Nd-YAG laser (Spectra-Physics Explorer ICD-532-200-E) operated at a repetition rate of 5 kHz was employed as the laser source for sintering. The pulse duration for the laser varies between 5 and 35 ns depending on the pulse repetition frequency. The laser beam was Gaussian with a beam waist diameter of 0.20 mm. Rest of the optics setup used was similar to the one used for the fs laser apparatus except that the objective used was a 40× microscope objective (NA-0.65).

**Continuous Wave Laser Setup.** For the CW laser setup, a 3 W diode pumped solid state laser laser (Lasever, Inc., Ningbo, China) with a central wavelength of 532 nm was employed. The laser beam was Gaussian with a beam waist diameter of 3 mm. The laser beam was focused through a 50× (NA-0.55) objective onto the samples through a couple of mirrors and mechanical shutter as

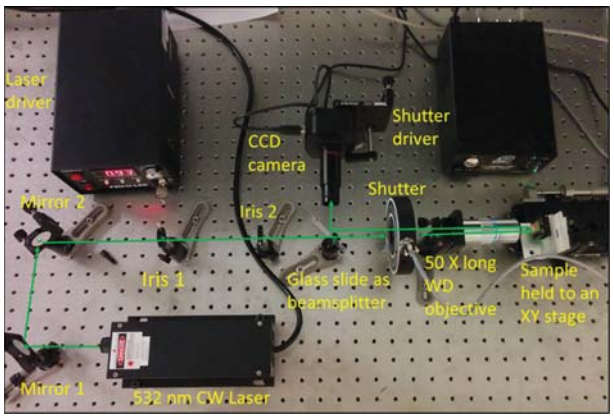


**Fig. 2 CW laser sintering setup**

shown in Fig. 2. The laser powers were measured using a thermal power measurement sensor (Ophir optronics,10A-P P/N 7Z02649) for power range 40 mW–10 W and using a photodiode sensor (Ophir optronics, PD 300 P/N 7Z02410) for powers up to 40 mW.

Three different thicknesses of Cu NPs were used in this research to study the effect of layer thickness on sintering fluence/irradiance of Cu NPs. Table 7 in the Appendix lists the spin coating parameters to achieve different thicknesses of Cu NP layers on aluminum and glass substrates. Thicknesses of Cu NP layers on both glass and aluminum substrates were kept to be the same and were measured to be 0.4±0.2 $\mu$m, 0.8±0.2 $\mu$m, and 1.2±0.2 $\mu$m using an optical profilometer (Wyko NT 9100).

## Theory

To estimate the energy required to sinter layer of NPs in the powder bed using the pulsed lasers, a simplified model of the sintering mechanism has been developed [5]. Overall, there are three fluence thresholds which are of interest for understanding the sintering of Cu NPs: (1) The onset of sintering threshold—fluence at which the necking between particles can be observed, (2) the melting threshold—fluence at which the particles melt, and (3) the ablation threshold—fluence at which particles vaporize. The energy thresholds required to sinter, melt, and ablate a spot size of diameter, $D$, and layer thickness, $h$, can be found using Eqs. (1)–(3) [8], respectively, where $f$ is the repetition rate, $\rho$ is the powder density, $C_P$ is the specific heat, $l_f$ is the heat of fusion, $l_v$ is the heat of vaporization, $T_i$ is the initial temperature of the powder bed, $T_f$ is the sintering temperature, and $A$ is the absorptivity of the powders

$$E_{\text{onset necking growth}} = \frac{\rho\pi D^2 h C_p (T_f - T_i)}{4A} \tag{1}$$

$$E_{\text{melting}} = \frac{\rho\pi D^2 h (C_p (T_f - T_i) + l_f)}{4A} \tag{2}$$

$$E_{\text{vaporization}} = \frac{\rho\pi D^2 h (C_p (T_f - T_i) + l_f + l_v)}{4A} \tag{3}$$

The corresponding threshold fluences are, therefore, given by

$$\text{fluence}_{\text{onset necking growth}} = \frac{\rho h C_p (T_f - T_i)}{A} \tag{4}$$

$$\text{fluence}_{\text{melting}} = \frac{\rho h (C_p (T_f - T_i) + l_f)}{A} \tag{5}$$

$$\text{fluence}_{\text{vaporization}} = \frac{\rho h (C_p (T_f - T_i) + l_f + l_v)}{A} \tag{6}$$

In this model, a few simplifying assumptions have been made. It is assumed that: (1) some properties of the NPs such as the specific heat capacity, heat of fusion, and heat of vaporization are the same as that of the bulk material; (2) threshold fluences (onset of sintering, melting, and ablation) are independent of exposure times as the time between each pulse is long enough so that particle bed returns to its initial state and past train of pulses do not affect the threshold fluences; (3) all of the laser energy during each pulse is expended in raising the temperature of the particles, i.e., there are no losses to the surroundings or neighboring particles; and (4) the NPs in the ink start sintering at 330 °C which have been observed [9] are much lower than the melting point of the bulk Cu. This means that the model does not capture all of the physics going on in the sintering process but it does provide a good initial estimate of the potential processing window for good sintering. This simple engineering model is, therefore, useful in determining the initial laser parameters around which the sintering process can be tuned to provide the best results.

For calculating the fluences accurately, estimates of physical and thermal properties including density, specific heat capacity, sintering onset temperature, heat of fusion, heat of vaporization, and absorptivity of Cu NP layer are required. Although melting of material occurs at bulk melting temperature for particles >10 nm in size, surface melting phenomenon can occur at much lower temperatures [22] and that is why the model assumes the melting temperature to be the same as sintering temperature. Thermal properties like specific heat capacity, heat of fusion, and heat of vaporization of Cu have been assumed to be the same as that of bulk Cu and have been taken from the literature (see Table 1). Other physical properties including density, absorptivity, thickness, and sintering temperature have been obtained experimentally.

## Nanoparticle Property Measurements

**Density Measurements.** Cu ink samples were spun on the substrate using the EZ6 spin coater, and weight measurements were taken using a symmetry PA analytical balance (Cole Parmer, Inc., Vernon Hills, IL) before and after (substrate with dried ink) the spin coating. The thickness of the layer was measured using a stylus profilometer (Dektak 6M). Coating area was estimated using the ImageJ image processing tool (see Fig. 3), and then, volume of the Cu nano-ink layer can be obtained as the product of the

**Table 1 Properties of Cu ink used for fluence calculations**

| Parameter | Value |
|---|---|
| $C_p$ | 385 J/kg K [25] |
| $T_i$ | 20 °C |
| $T_f$ | 330 °C |
| $l_f$ | 205 kJ/kg [25] |
| $l_v$ | 4796 kJ/kg [26] |
| $\rho$ | 3840±650 kg/m$^3$ |

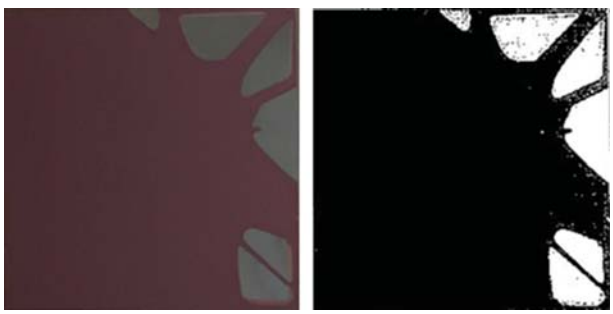

**Fig. 3 Area estimation using ImageJ**

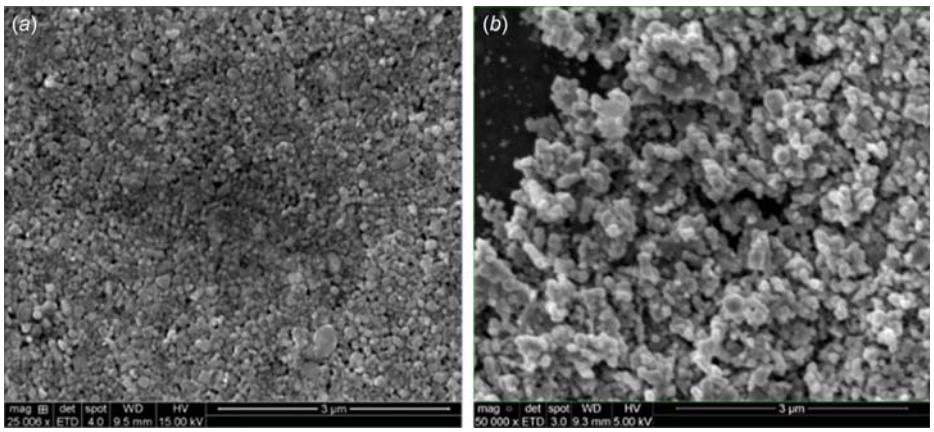


**Fig. 4 Comparison of morphology of Cu sample at (*a*) room temperature and (*b*) after heating till 350 °C**

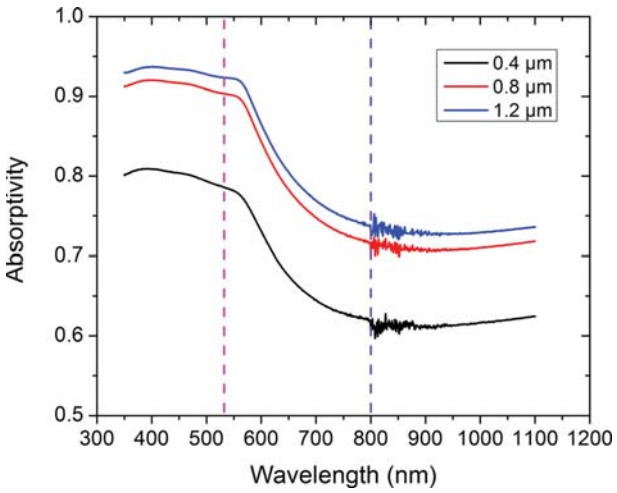


**Fig. 5 Absorptivity of Cu ink layer on glass substrate**

measured thickness and estimated area. The density of the spin coated ink layer was obtained to be $3.84 \pm 0.65$ g/cm$^3$.

**Sintering Temperature Determination.** Though the melting temperature of bulk Cu is 1085 °C, NPs have been observed to sinter [9,23] much below their bulk melting temperatures. Differential scanning calorimetry of the ink showed an exothermic peak at around 330 °C, indicating the onset of the sintering process [9]. Scanning electron microscope (SEM) images that were taken just before and after the exothermic peak (see Fig. 4) show the distinction between unsintered and sintered particles. The sample heated to 350 °C showed significant necking between the particles, and thus, validating the hypothesis that the exothermic peak at 330 °C corresponds to the onset of sintering. Therefore, 330 °C is used as the sintering temperature for modeling.

**Absorptivity Measurement.** Absorptivity of the Cu layers were obtained indirectly by measuring the reflectance and transmittance of the samples. A Cary 5000 UV-Vis-NIR (Agilent Technologies) was used to measure the transmittance and reflectance of a 150-nm thick Cu layers on glass substrate. To obtain the transmittance for the three Cu layer thicknesses included in the study, Beer–Lambert's law [24] given in Eq. (7) was used to obtain the absorption coefficient, and subsequently, the transmittance was obtained for 532 nm and 800 nm wavelengths by assuming that the absorption coefficient remains constant over the thickness range (0.15–1.2 $\mu$m)

$$I(z) = I_0 e^{-\alpha z} \tag{7}$$

$$T(z) = \frac{I(z)}{I_0} = e^{-\alpha z} \tag{8}$$

$I(z)$ denotes the intensity of light at depth $z$, $z$ denotes the propagation direction, $I_0$ is the initial amplitude of intensity, and $\alpha$ is the absorption coefficient. The reflectance data for the three-layer thicknesses were obtained using reflectance spectroscopy setup of the spectrophotometer, and finally, the absorptivity of the sample was obtained by subtracting the reflectivity and transmissivity from the overall normalized light intensity. Figure 5 shows the resultant absorptivity graph for different thicknesses of Cu layer on glass. Absorptivity graph for Cu layer on aluminum has been included in the Appendix.

Using the parameters listed in Table 1 and absorptivity of the sample, different threshold fluences were calculated at both 532 nm and 800 nm wavelengths of light and are listed in Tables 2 and 3 for glass and aluminum substrates, respectively. The slight difference in values between the fluence estimates for two substrates arises from the small difference in absorptivity of samples on these substrates at the previously-mentioned wavelengths. The values in the tables indicate the nominal fluence value for that

**Table 2 Estimated threshold fluences for 532 nm and 800 nm laser for glass substrate**

| Laser wavelength | Thickness ($\mu$m) | Onset of sintering (mJ/cm$^2$) | Melting (mJ/cm$^2$) | Vaporization (mJ/cm$^2$) |
|---|---|---|---|---|
| 800 nm | 0.4 | 31 (14–74) | 83 (37–202) | 1311 (587–3188) |
| | 0.8 | 52 (39–67) | 140 (105–183) | 2215 (1662–2891) |
| | 1.2 | 75 (64–88) | 205 (173–239) | 3232 (2731–3771) |
| 532 nm | 0.4 | 23 (11–51) | 63 (29–138) | 995 (452–2185) |
| | 0.8 | 41 (30–53) | 111 (81–143) | 1748 (1282–2260) |
| | 1.2 | 59 (49–70) | 161 (134–190) | 2537 (2114–2992) |

**Table 3 Estimated threshold fluences for 532 nm and 800 nm laser for aluminum substrate**

| Laser wavelength | Thickness ($\mu$m) | Onset of sintering (mJ/cm$^2$) | Melting (mJ/cm$^2$) | Vaporization (mJ/cm$^2$) |
|---|---|---|---|---|
| 800 nm | 0.4 | 29 (13–69) | 79 (36–187) | 1248 (562–2949) |
| | 0.8 | 52 (39–68) | 142 (105–186) | 2247 (1662–2935) |
| | 1.2 | 74 (61–87) | 202 (166–236) | 3188 (2622–3720) |
| 532 nm | 0.4 | 24 (11–51) | 64 (29–138) | 1008 (457–2185) |
| | 0.8 | 41 (30–53) | 111 (81–143) | 1748 (1282–2260) |
| | 1.2 | 59 (49–70) | 161 (134–190) | 2537 (2114–2992) |

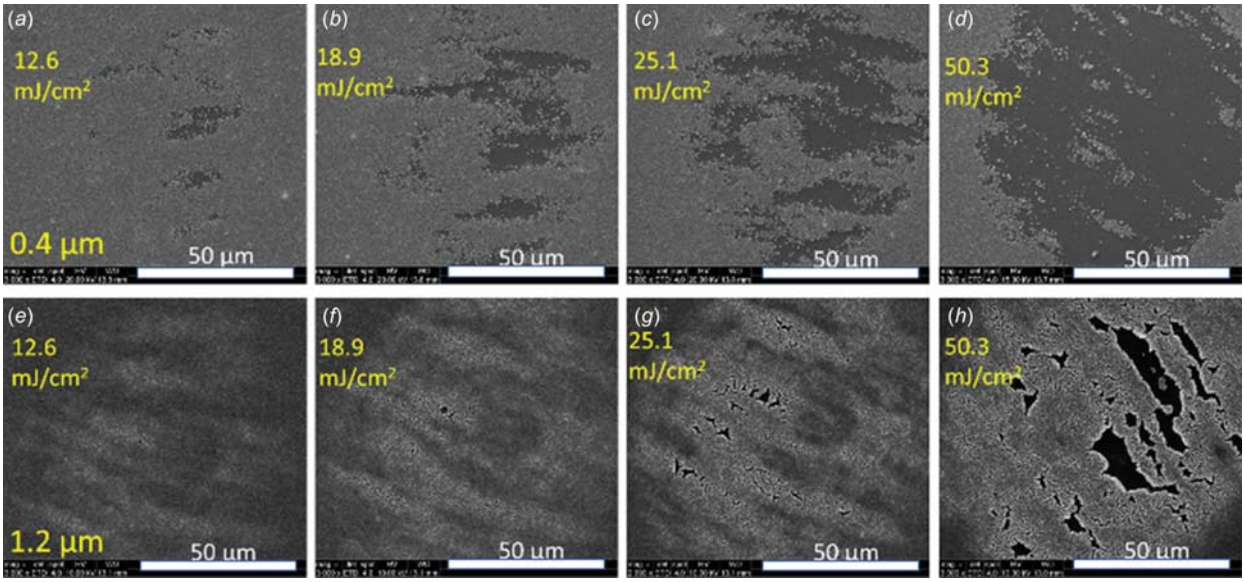


**Fig. 6 SEM images of spots sintered with (*a*) and (*e*) 12.6±2.9 mJ/cm$^2$, (*b*) and ( *f*) 18.9±4.3 mJ/cm$^2$, (*c*) and (*g*) 25.1±5.7 mJ/cm$^2$, (*d*) and (*h*) 50.3±11.2 mJ/cm$^2$ for 500 ms on 0.4 $\mu$m and 1.2 $\mu$m thick Cu layers on Al substrate**

thickness of Cu layer and the values in bracket indicate the 95% confidence interval of fluence estimate for that Cu layer thickness. For example, fluence range for the onset of sintering using fs laser (800 nm wavelength) for a 0.4 $\mu$m thick Cu layer on glass substrate was estimated to be between 14 and 74 mJ/cm$^2$. The primary factor of uncertainty in fluence estimate propagates from the uncertainty in thickness measurement of Cu layers. Uncertainty propagation for fluence estimates can be found in the Appendix.

## Sintering Results

**Femtosecond Laser Sintering.** For fs laser sintering, spot diameter for all samples (on both glass and aluminum substrate) was fixed at 90±10 $\mu$m. On aluminum substrate, laser powers between 2±0.3 mW (which equates to a fluence of 6.3±1.7 mJ/cm$^2$) and 16±0.3 mW (50.3±11.2 mJ/cm$^2$) were tested. Samples were exposed for 50 ms and 500 ms. With glass as the substrate, the powers were varied from 6±0.3 mW to 18±0.3 mW which correspond to a fluence range from 18.9±4.3 mJ/cm$^2$ to 56.6±12.6 mJ/cm$^2$. Figures 6–8 show the SEM images of fs laser sintered spots on aluminum and glass substrates.

Any misalignment between the optical elements in the system could lead to diffraction and interference effects from the edges of these optical elements and can lead to diffraction/interference patterns to appear on the sample as observed in these samples.

Sintering results from fs laser sintering on different substrates and different thicknesses have been condensed and represented as regions in Figs. 9 and 10. The pulsed laser sintering results (ns and fs lasers) have been classified into four broad categories: (1) no sintering: spots which were not affected by the incident laser power, i.e., no visible spot seen under the SEM (Fig. 11(*a*)); (2) weak sintering: spots which were partially affected by sintering and where some necking between particles could be observed. However, the extent of necking between particles was small and only a fraction of the spot area showed any necking between the particles. Figure 11(*b*) is one example of weak sintering; (3) good sintering: spots which showed significant necking between the particles and a majority portion of the spot area showed sintering (Fig. 11(*c*)); and (4) ablation/damage to the substrate: spots where a fraction or all of the spot area has been vaporized to reveal the substrate underneath, and in some cases, damaging the substrate as well (Fig. 11(*d*)).

Each row in Fig. 6 shows the SEM images of spots sintered with increasing powers on different Cu layer thicknesses (0.4 $\mu$m and 1.2 $\mu$m) on Al substrate for an exposure time of 500 ms. It can be observed that for the same fluence and same exposure time, spots fall into different categories (defined earlier) depending upon the layer thickness. Spot shown in Fig. 6(*b*) (Fluence—18.9±4.3 mJ/cm$^2$—0.4 $\mu$m thick Cu) is ablated, while the spot sintered with same fluence (see Fig. 6(*f*)) on a 1.2 $\mu$m thick Cu shows good sintering. Similar behavior is also observed with glass as the substrate (see Fig. 8). The trend of sintering threshold with thickness can be observed from the plots shown in Figs. 9 and 10. The sintering threshold increases slightly with increasing thickness of the Cu layer on either aluminum or glass substrate. Weak-good sintering window also expands with increasing Cu layer thickness. It is also interesting to note that, at lowest thickness of Cu layer, there is virtually no "good sintering" region.

With increasing exposure time, the extent of sintering improves as observed from Fig. 7 on Al substrate. In the figure, it is evident that more regions inside the spot are affected at longer exposure

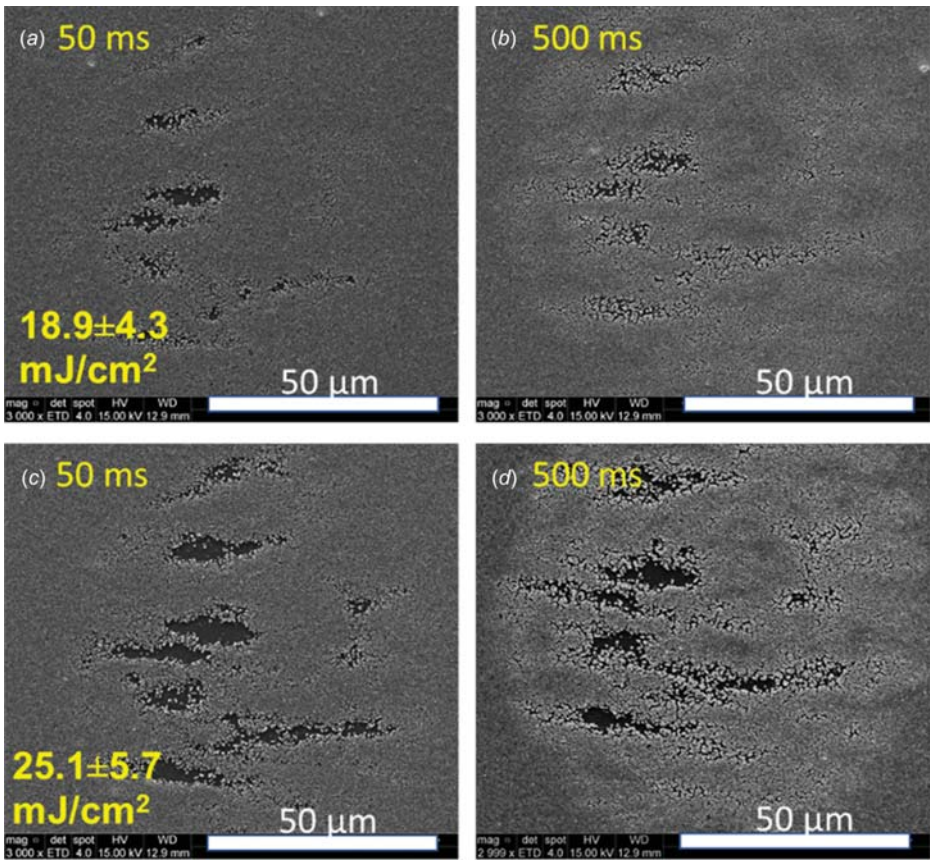


**Fig. 7 SEM images of spots sintered with 18.9±4.3 mJ/cm$^2$ for (*a*) 50 ms, (*b*) 500 ms, and with 25.1±5.7 mJ/cm$^2$ for (*c*) 50 ms, and (*d*) 500 ms on a 0.8 $\mu$m thick Cu layer on Al substrate**

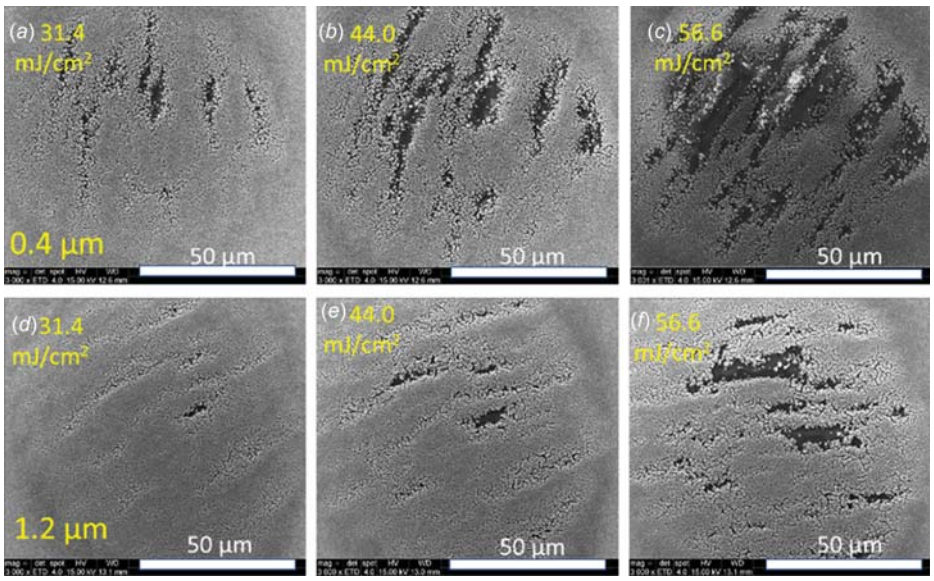


**Fig. 8 SEM images of FS sintered spots (*a*) and (*d*) 31.4±7.0 mJ/cm$^2$, (*b*) and (*e*) 44.0±9.8 mJ/cm$^2$, (*c*) and (*f*) 56.6±12.6 mJ/cm$^2$ for 500 ms on 0.4 $\mu$m and 1.2 $\mu$m thick Cu layers on glass substrate**

time compared to the spots with shorter exposure time. However, sintering and ablation thresholds do not vary much with exposure times as observed from the processing window plots. Material heating and cooling cycle for a fs laser can finish in a few picoseconds [27]. Thus, at a pulse repetition rate of 5000 Hz (interpulse duration—200 $\mu$s), the spot is already back to the room temperature before the next pulse hits the spot. For fluences lower than ablation threshold, current pulse improves the necking between the already necked particles (which have been initiated by previous train of pulses), and thus, enhances the sintering quality. For

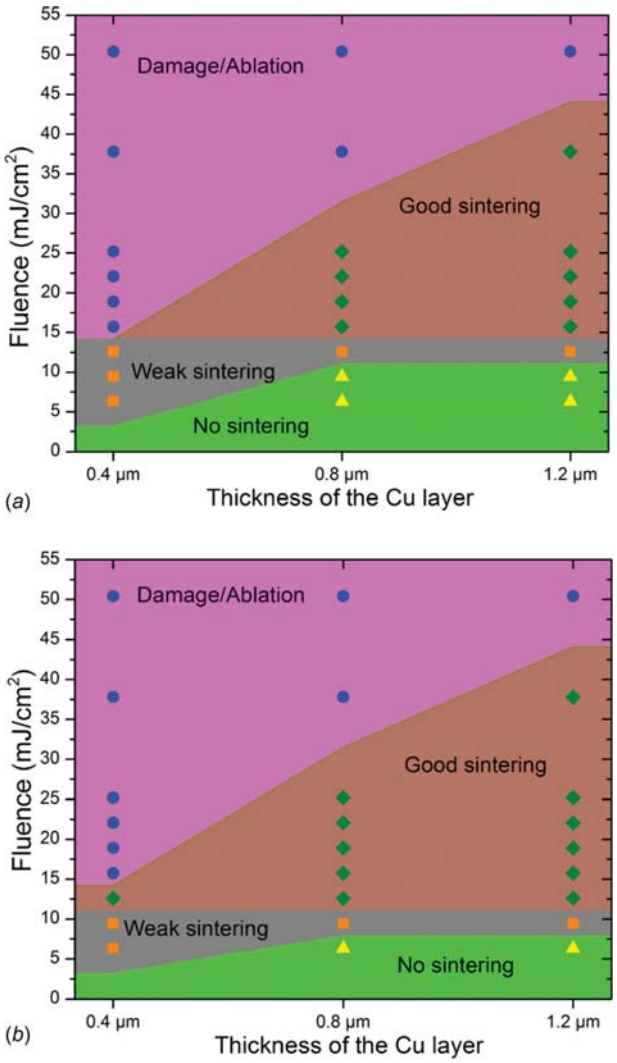


**Fig. 9 Processing window for different sintering regions for Cu samples on Al substrate: (*a*) 50 ms exposure and (*b*) 500 ms exposure**

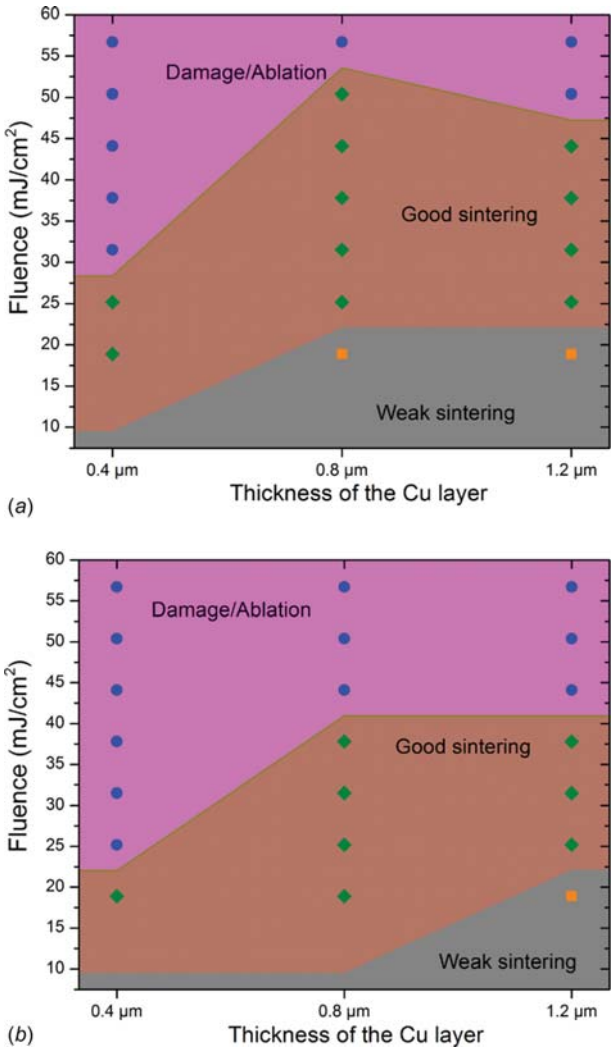


**Fig. 10 Processing window for different sintering regions for Cu samples on glass substrate: (*a*) 50 ms exposure and (*b*) 500 ms exposure**

fluences larger than ablation threshold, each pulse removes more and more material out of the spot. This explains why no significant effect of exposure time can be seen on the processing window.

Table 4 compares the onset of sintering and melting thresholds (from model) for different thicknesses of Cu layers on aluminum and glass substrates with the sintering window obtained from experimental data. From the model, it is expected that sintering will be observed between the onset of sintering and melting threshold. Overall, the experimental sintering window seems to be in good agreement with the predicted thresholds within margins of experimental error. The model is overestimating the thresholds slightly due to the fact that it uses specific heat capacity, heat of fusion, and heat of vaporization of the bulk material instead of that for NPs. Nanoparticles of metals such as tin have been reported to show a lower heat of fusion than their bulk counterparts by over 50% depending upon the size of NPs [28,29]. However, the change in the thermodynamic properties of Cu as a function of NP size is not well known which leads to this overprediction.

Experimental sintering window along with ablation thresholds is nearly the same for both substrates suggesting that sintering and ablation thresholds are independent of the thermal diffusivity of the material for the fs laser sintering. Previous studies have reported the melting fluence of Cu NPs (diameter-10 nm) using a fs laser (800 nm, 100 fs pulse duration) of 12.8 mJ/cm$^2$ [6] and ablation threshold using a (248 nm, 500 fs pulse duration) fs laser to be 170 mJ/cm$^2$ [30]. For the three thicknesses used in this study, the damage threshold varies between 14.2 mJ/cm$^2$ and 53.5 mJ/cm$^2$ depending on the thickness of the Cu layer (see Figs. 9 and 10). This shows good agreement of the results with the previously reported values.

**Nanosecond Laser Sintering.** The spot size for ns laser sintering experiments was fixed at $100\pm10$ $\mu$m for all thicknesses and substrates. Laser power was varied between $10\pm5$ mW and $140\pm10$ mW which corresponds to a fluence range of $25.5\pm14$ mJ/cm$^2$ and $357\pm76$ mJ/cm$^2$ for both aluminum and glass substrates. Exposure times of 50 ms and 500 ms were used. Figures 12 and 13 show the SEM images of sintered samples on aluminum substrate and on glass substrate, respectively.

The complete sintering window for ns laser sintering has been depicted in Figs. 14 and 15. Sintering spots have been characterized into the same four categories defined earlier for the fs laser sintering: (1) no sintering, (2) weak sintering, (3) good sintering, and (4) ablation/damage.

Scanning electron microscope images in Fig. 12 (aluminum) and Fig. 13 (glass) show the progression of sintering with

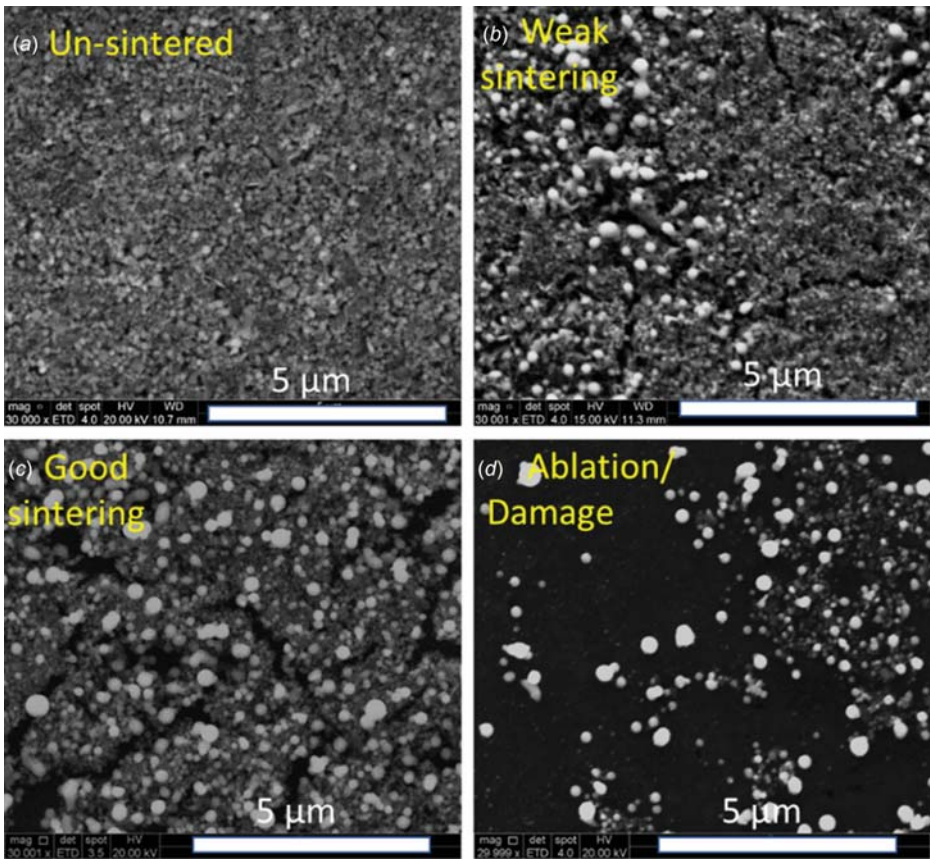


**Fig. 11 Morphology of pulsed laser sintered spots classified into different categories of processing window: (*a*) no sintering, (*b*) weak sintering, (*c*) good sintering, and (*d*) ablation/ damage**

**Table 4 Comparison of the experimental sintering window with model predictions**

| Substrate | Thickness ($\mu$m) | Onset of sintering (mJ/cm$^2$) | Melting (mJ/cm$^2$) | Experimental sintering window (mJ/cm$^2$) |
|---|---|---|---|---|
| Aluminum | 0.4 | 29 (13–69) | 79 (36–187) | 3.2–14.2 |
| | 0.8 | 52 (39–68) | 142 (105–186) | 11.0–31.5 |
| | 1.2 | 74 (61–87) | 202 (166–236) | 11.0–44.1 |
| Glass | 0.4 | 31 (14–74) | 83 (37–202) | 4.7–28.4 |
| | 0.8 | 52 (39–67) | 140 (105–183) | 4.7–53.5 |
| | 1.2 | 75 (64–88) | 205 (173–239) | 4.7–47.2 |

increasing power and the comparison between different thicknesses of Cu layers. Looking at the SEM images and plots showing the sintering regions, it is evident that the thresholds for all the four categories increase with increasing thickness of the Cu layer. This behavior is observed with both substrates. Also, the good sintering window also becomes wider with increasing thickness of Cu layer, the same trend it demonstrated with fs laser sintering. Variations in different thresholds with changing exposure times are insignificant. Weak-good sintering window from the experimental data matches quite well with the predicted fluence window between the onset of sintering and melting thresholds (see Table 5).

Theoretical ablation fluence for bulk Cu films using a 532-nm ns laser has been reported to be between 3.28 and 6 J/cm$^2$ [31,32]. Experimental studies have reported the Cu film ablation threshold to be 1.61 J/cm$^2$ [31] which is lower than the theoretical threshold. This discrepancy is due to the fact that the theoretical model [32–34] is based on thermal model of vaporization and does not take into account the effects of plasma ignition which aids ablation, thus reducing the fluence requirement for ablation. The experimental ablation threshold in this study varies between 63.5 and 331 mJ/cm$^2$ depending upon the thickness of Cu layer. This is 10–100 times smaller than the previously reported theoretical estimate and 5–25 times smaller than the experimental results reported in the literature for Cu thin films. This difference can be explained by the fact that the theoretical model estimate and the experimental data reported in the literature were for bulk Cu films and not for Cu NP beds. Nanoparticles due to their high surface area to volume ratio and high surface energies exhibit properties which are completely different from bulk properties including low melting point and enhanced absorption due to surface plasmon resonance which is absent in bulk Cu. Cu NPs show a strong absorption peak near 570 nm [35] which can also be corroborated by the absorption curves presented earlier in this study. This peak is a result of the surface plasmon resonance band which have been observed between 560 nm and 580 nm [36]. This is close to the wavelength of the ns laser (532 nm), and thus, a higher absorption by the NPs is observed compared to the bulk Cu film. Besides

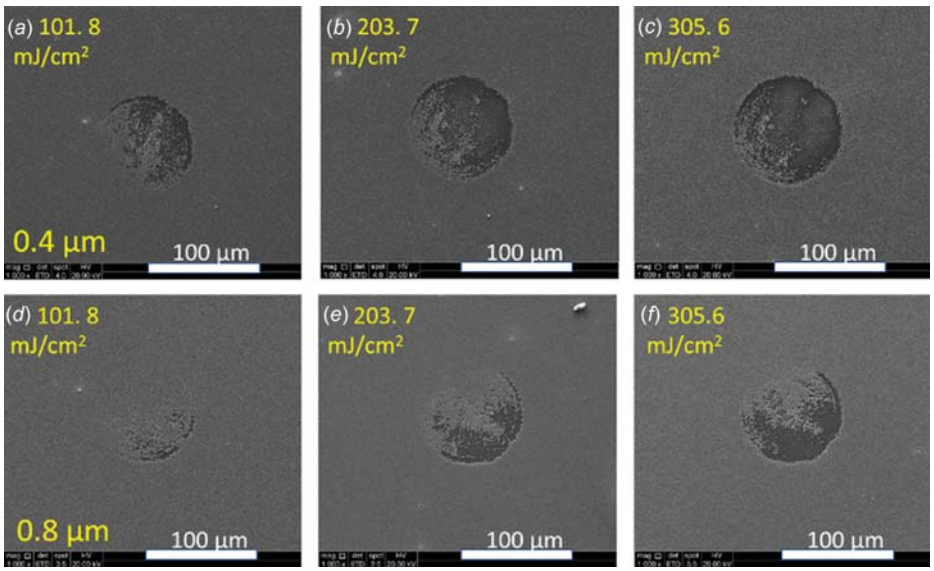


**Fig. 12 SEM images of spots sintered with (*a*) and (*d*) 101.8±24.0 mJ/cm², (*b*) and (*e*) 203.7±48.0 mJ/cm², (*c*) and (*f*) 305.6±66.2 mJ/cm² for 500 ms on 0.4 μm and 0.8 μm thick Cu layers on Al substrate**

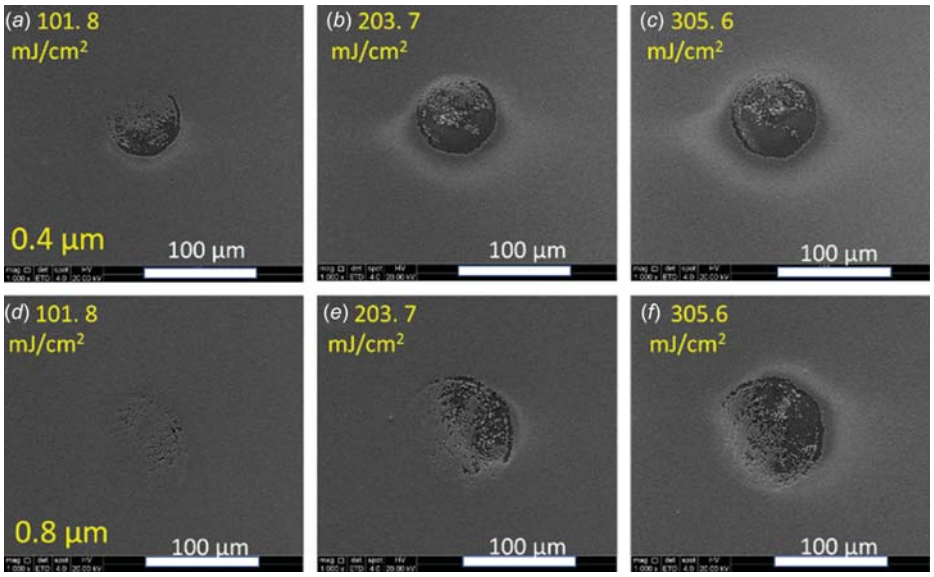


**Fig. 13 SEM images of spots sintered with (*a*) and (*d*) 101.8±24.0 mJ/cm², (*b*) and (*e*) 203.7±48.0 mJ/cm², (*c*) and (*f*) 305.6±66.2 mJ/cm² for 500 ms on 0.4 μm and 0.8 μm thick Cu layers on glass substrate**

enhanced absorptivity, the thermal conductivity of NPs is poor compared to the bulk material [37,38]. This leads to lower conduction losses, and thus, aiding NP melting at very low energy levels. In addition, melting temperature depression enables ablation driven by vaporization at much lower laser energy than bulk. The cumulative effect of all these factors causes a significant reduction in actual ablation threshold as observed in this study.

Balling up of NPs was another phenomenon which was significantly higher with ns laser sintering compared to fs laser sintering. Balling occurs when the NP melt pool is unstable, i.e., when the total surface of the melt pool is larger than the surface area of a sphere with same volume, the melt pool tends to ball up [39]. This effect is more prominent with ns laser as compared to fs laser because the pulse duration is long enough that it allows the formation of melt pool and because the interaction between ns laser and material is thermal in nature. On the other hand, the interaction of fs laser with matter is largely electrostatic and is hardly affected by the thermal transport mechanisms [18] or by hydrodynamic effects.

It is also interesting to note that samples on both aluminum and glass substrates demonstrated similar experimental threshold fluences with both fs and ns lasers. With fs laser, as the pulse duration is smaller than the lattice heating time [18], there is no chance of conduction between the particles and the substrate, and hence, no effect of substrate diffusivity is expected. When the timescales are longer than lattice heating time, heat penetration depth is given by

$$h_d = \sqrt{\kappa * t} \tag{9}$$

where $\kappa$ is the thermal diffusivity of the material and $t$ is the pulse duration of the ns laser. For bulk Cu, thermal diffusivity is

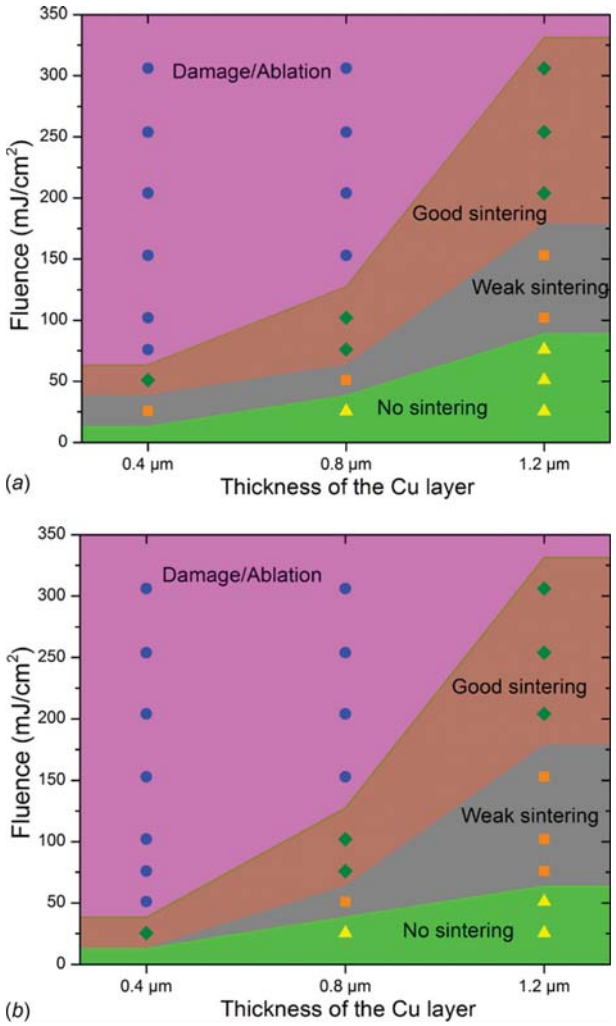


**Fig. 14 Processing window for different sintering regions for Cu samples on Al substrate: (*a*) 50 ms exposure and (*b*) 500 ms exposure**

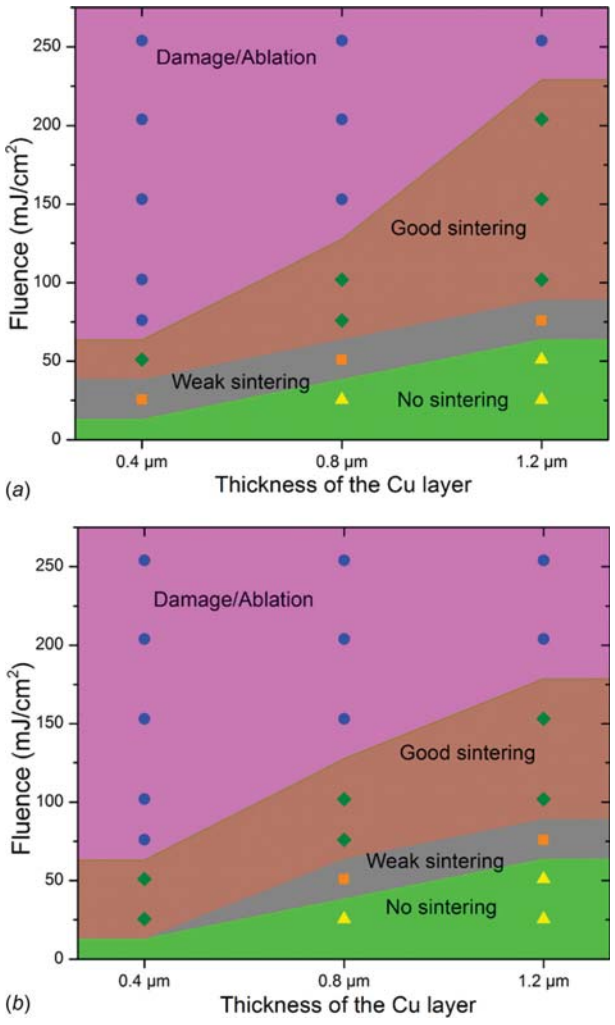


**Fig. 15 Processing window for different sintering regions for Cu samples on glass substrate: (*a*) 50 ms exposure and (*b*) 500 ms exposure**

111 $mm^2/s$ [40] and with a pulse duration of 25 ns, thermal penetration depth comes out to be 1.6 $\mu$m which is larger than the layer thicknesses used in this study. However, due to porous nature of NP bed compared to the bulk, thermal diffusivity of the NPs can be significantly smaller, and thus, the penetration depth might be on the same order and in some cases even smaller than the thickness of the layer thus making the role of substrate's thermal diffusivity in conduction of heat minimal. And that explains why similar thresholds were observed with both substrates using ns laser.

The model presented earlier does a good job in predicting the sintering window (window between the onset of sintering fluence and melting fluence) for both fs and ns lasers within the limits of experimental error. It works well for fs laser estimation because there is insignificant heat diffusion into the surrounding during the pulse's timescale, and thus, the assumption in the model that there are no losses seems valid for the fs laser sintering. The predictions are slightly larger than the actual sintering window due to the bulk material property assumptions mentioned earlier.

For ns laser, the predictions do not consider the losses due to heat transport (conduction), and thus, the model estimates should be lower than the actual sintering window results. Conduction losses become significant when pulse duration is larger than lattice heating time [41]. Lattice heating time is on the order of picoseconds, and hence, conduction is a major source of losses for ns laser sintering [18]. However, the model uses specific heat capacity and heats of fusion of bulk material which contribute to overestimation of threshold of onset of sintering and melting, and thus, inflating the estimate. Due to the overall effect of these competing factors, the model estimates the sintering window with good agreement with the experimental data.

Vaporization thresholds predicted by the model (see Tables 2 and 3) are one order of magnitude higher than the actual ablation thresholds observed with both fs and ns lasers on both substrates. In fact, ablation was quite significant with fluences larger than the melting fluence thresholds. This behavior of NPs can be explained by the fact that NPs of metals [42] and alloys [43] (GeTe nanowires) have been reported to have enhanced sublimation much below their melting points. At elevated temperatures, the vapor pressure of small metal NPs can be orders of magnitude higher than that of the bulk metal which leads to a reduced heat of vaporization. And, thus, the actual heat required for vaporization of NPs would be much lower than the heat of vaporization of bulk metal which has been used in the model. This explains the reason for ablation of particles much below the fluence corresponding to vaporization of bulk material. Overall, a better measure of the heat of vaporization of Cu NPs is needed to make an accurate estimate of the vaporization threshold.

Overall, despite using some of the physical properties of the bulk material like specific heat capacity, heat of melting, and heat

**Table 5 Comparison of the experimental sintering window with model predictions**

| Substrate | Thickness ($\mu$m) | Onset of sintering (mJ/cm$^2$) | Melting (mJ/cm$^2$) | Experimental sintering window (mJ/cm$^2$) |
|---|---|---|---|---|
| Aluminum | 0.4 | 24 (11–51) | 64 (29–138) | 12.8–63.5 |
| | 0.8 | 41 (30–53) | 111 (81–143) | 38.25–127.5 |
| | 1.2 | 59 (49–70) | 161 (134–190) | 89–331.5 |
| Glass | 0.4 | 23 (11–51) | 63 (29–138) | 12.8–63.5 |
| | 0.8 | 41 (30–53) | 111 (81–143) | 38.25–127.5 |
| | 1.2 | 59 (49–70) | 161 (134–190) | 63.5–229 |

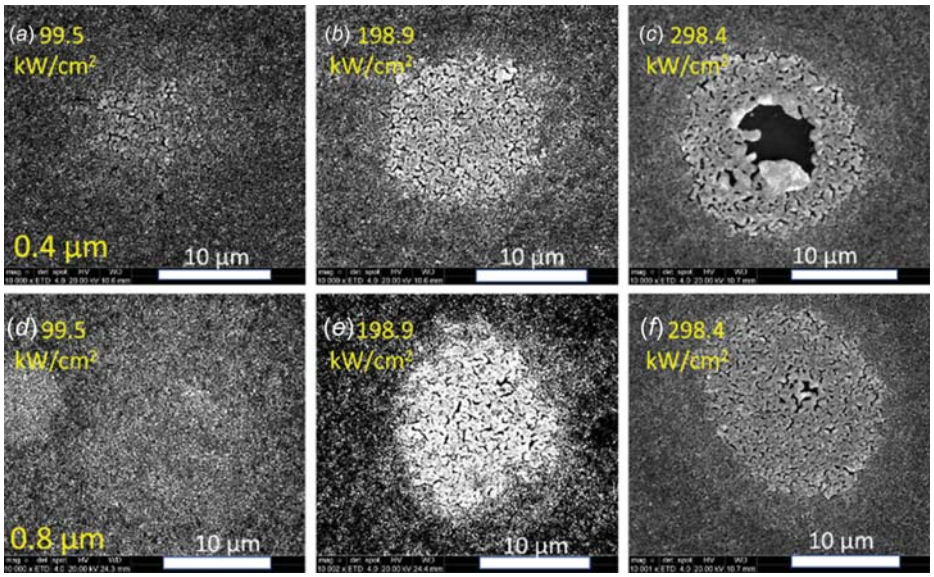


**Fig. 16 SEM images of spots sintered with power density: (*a*) and (*d*) 99.5±37.6 kW/cm$^2$, (*b*) and (*e*) 198.9±75.3 kW/cm$^2$, (*c*) and (*f*) 298.4±112.3 kW/cm$^2$ ms for 500 ms on 0.4 $\mu$m and 0.8 $\mu$m thick Cu layers on Al substrate**

of vaporization, the simple thermodynamic model presented in this paper still provides good estimate of the onset of sintering fluence for the Cu NPs using fs and ns laser sources. However, to get a more accurate estimate of the fluence level for ablation, it would be desirable to find and employ the thermal properties of the NPs. Another limitation of this model is that it only uses the principle of conservation of energy and does not differentiate between the different modes of heat transfer, i.e., conduction, convection, and radiation. Thus, a more rigorous approach which uses the laser-NP interaction mechanisms can be used to get better estimates of the sintering and ablation thresholds. Since the model does not consider the heat transport between NPs, this model will not be effective in estimating the sintering fluence for continuous wave lasers as there is considerable heat being lost due to all three modes of heat transfer when longer duration heat sources are used for the sintering process.

**Continuous Wave Laser Sintering.** For CW laser sintering on a glass substrate, the spot size was fixed at 28±5 $\mu$m using a 50× long working distance objective. Due to high power density requirements for sintering of Cu NPs on aluminum substrate, the spot size on aluminum substrates had to be fixed at 16±3 $\mu$m. Fluence is defined as the pulse energy density hitting the sample surface, i.e., pulse energy of the laser divided by the area of the spot. A CW laser, however, is a continuous laser beam and does not have pulses. For CW lasers, irradiance, also called as power density, can be thought of as the counterpart to fluence (associated with pulsed lasers). It is defined as the average power of the laser divided by the spot size. In this study, irradiance was used as the control parameter for CW laser sintering. For glass substrate, powers ranging from 10±3 mW to 300±10 mW were tested. This power range corresponds to an irradiance range from 1.62±0.76 kW/cm$^2$ to 48.72±17.48 kW/cm$^2$. For sintering on aluminum substrate, laser powers varying from 100±10 mW to 1500±50 mW corresponding to an irradiance range of 49.73±19.30 kW/cm$^2$ to 746.04±280.87 kW/cm$^2$ were tested. With ns and fs lasers, it was postulated that the exposure times will not affect the various thresholds much as the pulse durations were very small compared to the heat diffusion time (in the case of fs lasers) and the time between pulses was long enough compared to the pulse durations, and thus, past train of pulses did not affect the sintering characteristics, i.e., there was no accumulation effect between the pulses. This hypothesis does not work with CW lasers as the laser is hitting the surface continuously for the exposure duration and energy is being accumulated in the material which causes different phenomena such as sintering and melting of NPs. Thus, to get an accurate understanding of the dependence of these thresholds on the exposure time, four different exposure times were used for the CW laser sintering—10 ms, 50 ms, 200 ms, and 500 ms. Figures 16 and 17 show the SEM images of CW laser sintered samples on aluminum and glass substrates, respectively. All the spots have been classified into four categories: (1) no sintering (see Fig. 18(*a*) for reference), (2) weak sintering (Fig. 18(*b*))—some sintering across the spot area but sintering is not uniform across the spot, (3) good sintering (Fig. 18(*c*))—significant necking between the particles and sintering is uniform throughout the spot, and (4) melting: NPs melt to form a visible melt pool (Figs. 16(*c*) and 18(*d*)) and the hydrodynamics of the melt pool forced it toward the periphery of the spot

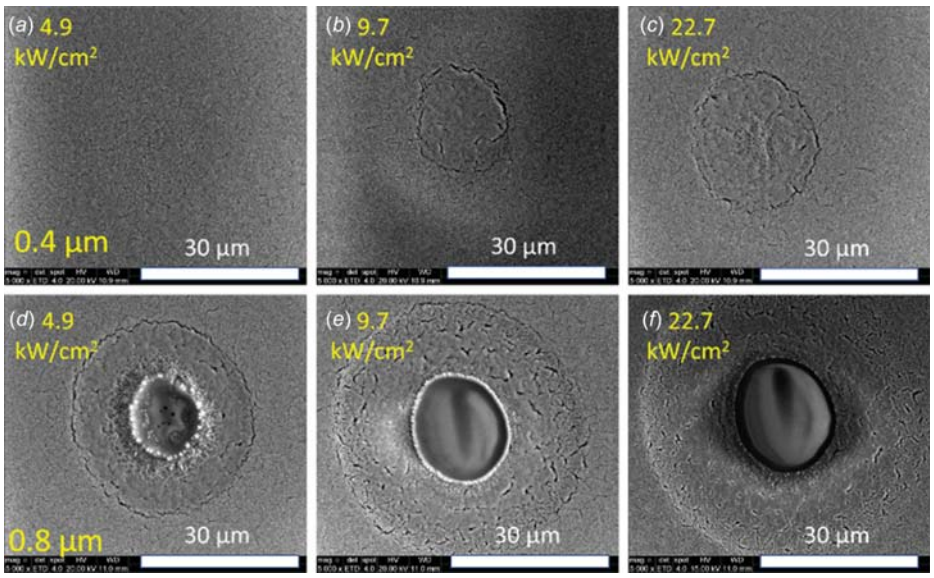


**Fig. 17 SEM images of spots sintered with power density: (*a*) 4.9±1.9 kW/cm$^2$, (*b*) 9.7±3.6 kW/cm$^2$, (*c*) 22.7±8.3 kW/cm$^2$ on 0.4 μm thick Cu layer, (*d*) 4.9±1.9 kW/cm$^2$, (*e*) 9.7±3.6 kW/cm$^2$, and (*f*) 22.7±8.3 kW/cm$^2$ for 500 ms on 0.8 μm thick Cu layer on glass substrate**

(Fig. 18(*d*)) shows the edge of the spot where melt pool can be seen accumulated). Instead of having ablation as one of the categories, melting was selected because the irradiance requirement for the ablation of NPs using CW lasers is extremely high, and due to the limitations of the experimental setup, the ablation of Cu NPs using CW laser could not be observed.

Plots in Figs. 19 and 20 show different regions in the processing window for samples sintered with CW laser on glass and aluminum substrates. Figures 16 and 17 show the SEM images of spots sintered with increasing powers on different thicknesses (with constant exposure time) for aluminum and glass substrates, respectively. From the SEM images on both substrates and the plots shown in Figs. 21 and

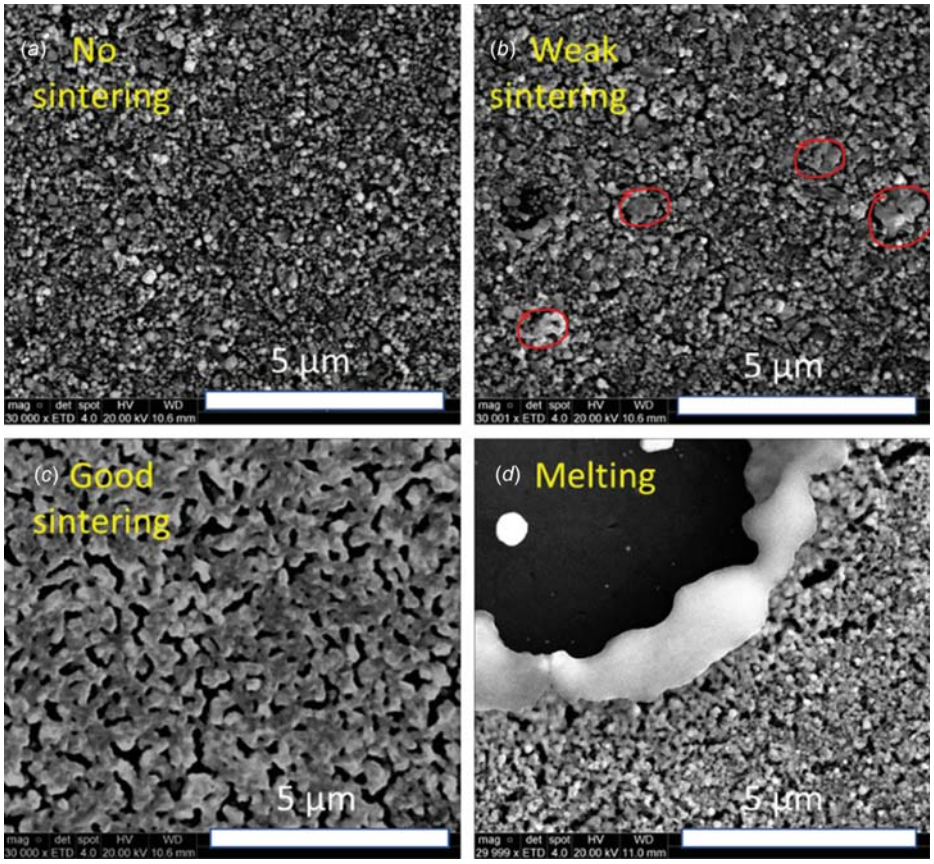


**Fig. 18 Morphology of CW laser sintered spots classified into different categories of processing window: (*a*) no sintering, (*b*) weak sintering, (*c*) good sintering, and (*d*) melting**

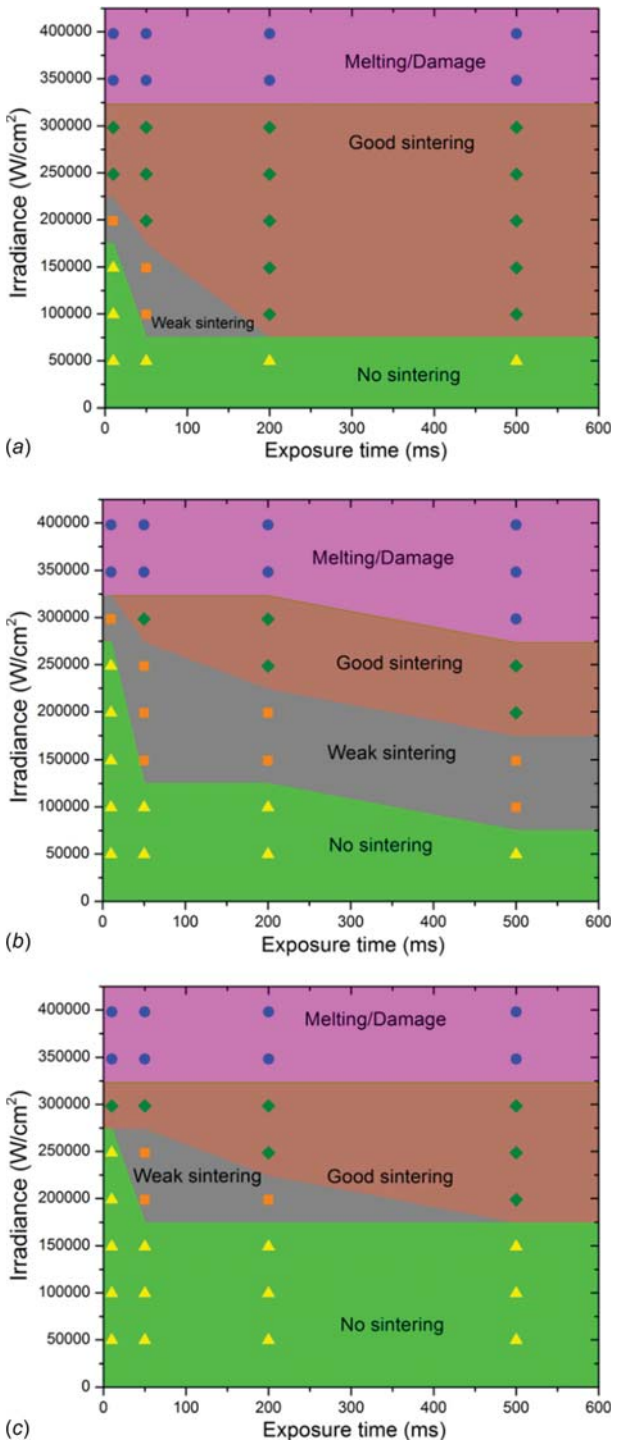


**Fig. 19 Processing window for different sintering regions for Cu samples on Al substrate: (*a*) 0.4 $\mu$m, (*b*) 0.8 $\mu$m, and (*c*) 1.2 $\mu$m thick Cu layer**

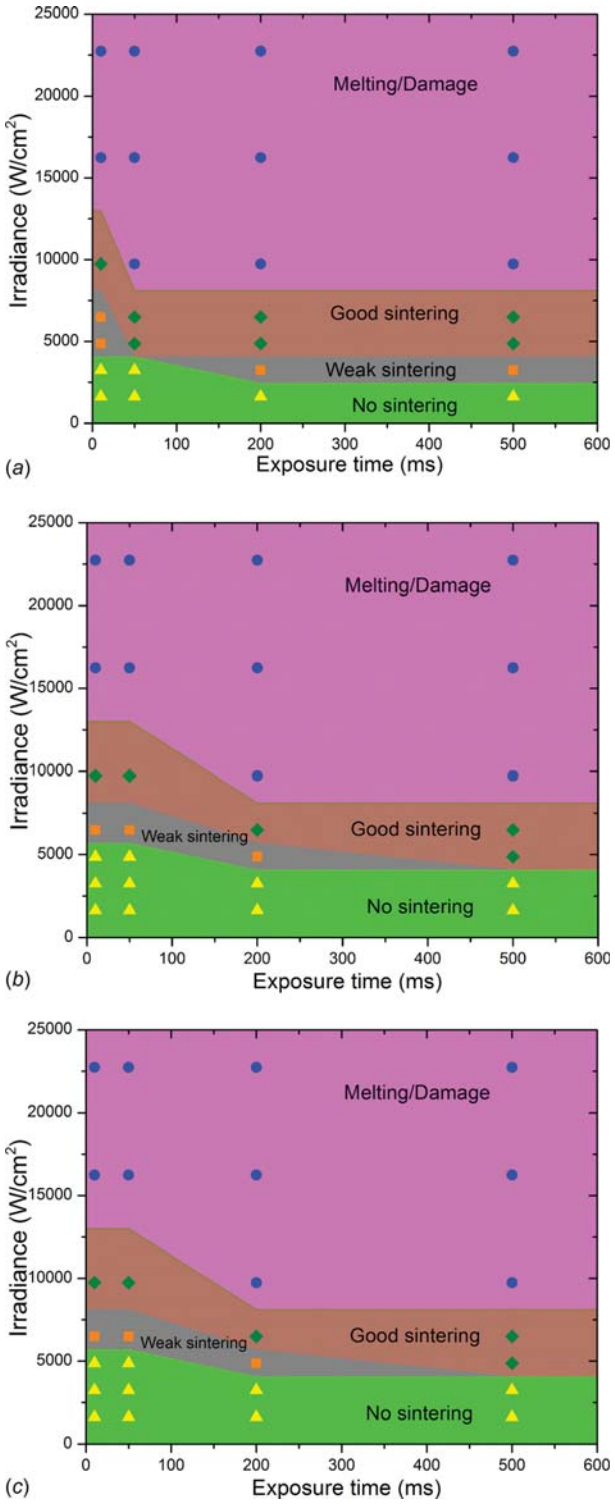


**Fig. 20 Processing window for different sintering regions for Cu samples on glass substrate: (*a*) 0.4 $\mu$m, (*b*) 0.8 $\mu$m, and (*c*) 1.2 $\mu$m thick Cu layer**

22, the sintering thresholds are observed to increase with increasing thickness. With respect to exposure time, the irradiance thresholds generally increase with decreasing exposure time except a few anomalies. For example, the melting threshold appears to be constant with exposure time for 0.4 $\mu$m and 1.2 $\mu$m thick samples on aluminum substrates. SEM images in Fig. 23 show the change in sintering behavior with exposure time at a constant irradiance for aluminum and glass substrates, respectively. This trend seems to be consistent across different thicknesses and substrates. On comparing the higher magnification images of the CW laser sintered spots (see Fig. 18) with the ones sintered using short pulsed lasers (see Fig. 11), it is evident that the quality of sintering observed with CW lasers is much better in terms of uniformity of sintering across the spot area. It was also observed that the balling phenomenon which was significant with ns laser was hardly observed with CW laser sintering. The continuity of laser beam over a single spot for the entire duration of exposure time prevents localized spheroidization of NPs. Another major difference between the CW laser sintered spots and pulse laser

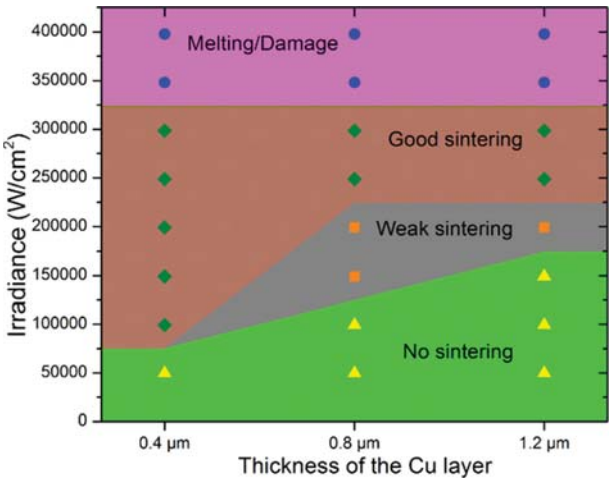


**Fig. 21 Processing window for different sintering regions for Cu samples on Al substrate for 200 ms**

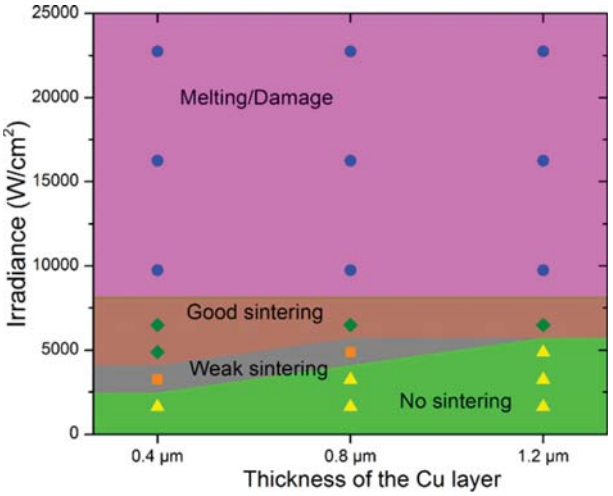


**Fig. 22 Processing window for different sintering regions for Cu samples on glass substrate for 200 ms**

sintered spots is the heat-affected zone in the two cases. With pulsed lasers, the spot boundaries were well defined and the adjoining regions were hardly affected, especially with fs laser sintered spots. On the other hand, CW laser sintered spots have considerably large heat affected areas around the spot and this heat affected zone grows with the increasing exposure time as can be observed from the SEM images in Fig. 23.

The cross-sectional SEM image of the sintered spot (Fig. 24(*b*)) shows significant sintering between particles across layers, whereas the particles across layers can be seen distinct from one another in an unsintered spot. It is imperative that all particles across the thickness of the layer are adequately sintered to ensure desirable mechanical and electrical properties of the sintered part.

## Discussion

From the compiled data for all the laser sintered spots, it is evident that the power requirements with CW laser sintering are much higher compared to those with pulsed laser sintering. Table 6 lists the fluence/irradiance sintering windows (weak-good sintering regions) for aluminum and glass substrates using all the three lasers. The values in the table indicate the minimum fluence/irradiance and maximum fluence/irradiance (with uncertainties) across different thicknesses to achieve sintering of NPs. For pulsed lasers, average irradiance levels have also been presented in addition to the fluences, so that the comparison with CW laser becomes easier. From the table, it can be observed that the sintering irradiance threshold is highest for the CW laser followed by ns laser and then by fs laser. Range of irradiances for sintering is also the widest for CW laser, and then, followed by ns and fs lasers in that order.

It is interesting to observe that the effect of thermal diffusivity of the substrate material on the sintering threshold and sintering window is significantly observable only with CW laser sintering. The large difference in sintering thresholds for samples with aluminum and glass substrates can be attributed to the difference in diffusivity of glass and aluminum. Aluminum with a higher diffusivity allows heat to diffuse through it easily as compared to glass. With CW laser sintering, there is a constant supply of heat for 10–500 ms (exposure times used in this study) which is sufficient for the heat to travel through the NP layer (time taken is on the order of few tens of nanoseconds depending upon the effective thermal diffusivity of Cu NPs—see Eq. (9)) to the substrate, and then, the substrate acts as a heat sink. A substrate with high

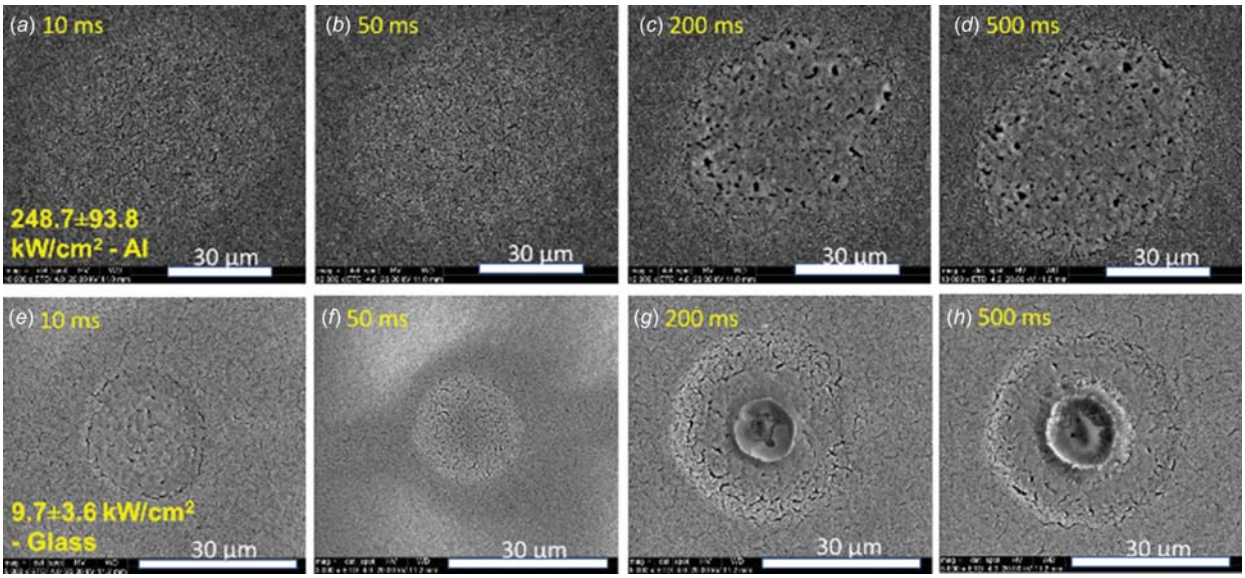


**Fig. 23 SEM images of spots sintered with power density 248.7±93.8 kW/cm² for (*a*) 10 ms, (*b*) 50 ms, (*c*) 200 ms, and (*d*) 500 ms on 1.2 μm thick Cu layer on Al and with 9.7±3.6 kW/cm² for (*e*) 10 ms, (*f*) 50 ms, (*g*) 200 ms, and (*h*) 500 ms on 0.8 μm thick Cu layer on glass substrate**

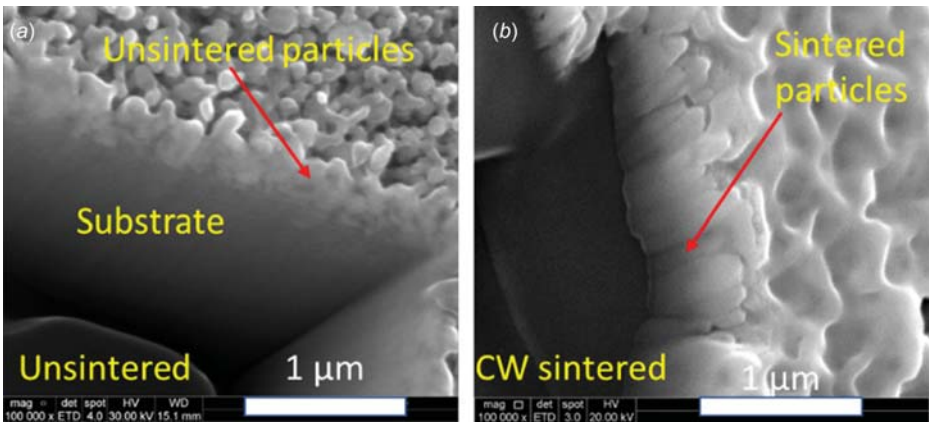


**Fig. 24 SEM images of cross sections of an unisntered and CW laser sintered spot**

**Table 6 Comparison of the experimental sintering window for FS, NS, and CW lasers**

| | | Substrate | |
|---|---|---|---|
| Type of laser | | Aluminum | Glass |
| FS | Fluence | 3.2±1.7–44.1±8.4 | 4.7±2.2–53.5±11.9 |
| | Average irradiance | 15.7±8.5–220±42 | 23.6±11–267±59 |
| NS | Fluence | 12.8±6.3–331±70 | 12.8±6.3–229±53 |
| | Average irradiance | 64±32–1655±350 | 64±32–1146±262 |
| CW | Average irradiance | 74,603±19,302–323,283±112,347 | 2436±1204–12,992±4632 |

Note: All fluences are in mJ/cm$^2$ and irradiances are in W/cm$^2$.

thermal diffusivity (aluminum) dissipates the heat, inhibiting the sintering process and a substrate with low thermal diffusivity (glass) stores the heat to raise the bed temperature, and thus, aiding the sintering process. Thus, samples on aluminum substrate require much higher irradiance for sintering of NPs than are required for samples on glass substrate. The effect of substrate diffusivity does not seem to significantly affect the sintering with pulsed lasers (fs and ns) due to the fact that pulse times are shorter than time it takes then heat to diffuse within the powder bed.

## Conclusion

In this paper, we have presented the sintering processing window for Cu NPs using different laser sources (fs, ns, and CW lasers). A comprehensive investigation was carried out to identify regions of: (1) no sintering, (2) weak sintering, (3) good sintering, and (4) ablation/melting in the processing window for each of the different lasers. The variation of these regions with thickness of the Cu layers and exposure times was also studied and identified. This study showed that both pulsed and CW lasers have their own advantages and disadvantages. With pulsed lasers, the heat-affected zones are minimal but their processing window is narrow and requires a tight control on the processing parameters to achieve good sintering. On the other hand, CW lasers provide a much larger processing window and flexibility in control parameters, and the sintering quality is also better in terms of uniformity of sintering across the spot. However, it suffers from heat diffusion and can have significantly larger heat-affected zones depending upon the exposure time. This knowledge of optimum sintering windows for Cu NPs using different lasers will prove to be extremely helpful for researchers trying to use Cu NPs for the additive manufacturing of electronic structures.

This paper also presented a simplified model to estimate the ideal sintering window for metal NPs using pulsed lasers. Based on the analysis of experimental results obtained from fs and ns laser sintering of Cu NPs, the model seems to be in good agreement with the experimental data within the margins of experimental error. This simplified model can thus prove to be extremely useful in identifying the maximum power requirement for sintering based on desired throughput from the tool which is required to design systems/tools that employ pulsed laser sintering of metal NPs.

The model accuracy (especially for vaporization thresholds) could be improved by using effective properties of the NP bed instead of the bulk material properties such as specific heat capacity, heat of fusion, and heat of vaporization. Another scope of improvement in the model could be to consider the different modes of heat transfer between NPs and between NPs and the surroundings in the energy conservation equation. A more rigorous approach that uses the laser-NP interaction mechanisms could help to get better estimates of the sintering and ablation thresholds. Further studies may be conducted to investigate the mechanical and electrical properties of good sintered spots and identify the correlations between these properties and sintering processing parameters. The hypothesis regarding the role of substrate diffusivity on sintering processing window which was verified in this study with two substrates can also be corroborated and consolidated by conducting experiments with substrates having a range of thermal diffusivities.

## Acknowledgment

The authors would like to acknowledge the financial support received from NXP Semiconductors. The authors would like to thank Mr. C. S. Foong and Mr. Leo Higgins of NXP Semiconductors for their valuable inputs to the discussion on the sintering experiments.

## Funding Data

- NXP Semiconductors.

## Appendix

See Table 7, Figs. 25–36, and Equations.

Table 7 Spin coating parameters

| S. no | Substrate | Speed (rpm) | Time (s) | Acceleration (rpm/s) | Thickness ($\mu$m) |
|---|---|---|---|---|---|
| 1 | Aluminum | 1000 | 10 | 200 | 0.4±0.2 |
| | | 6000 | 30 | 1000 | |
| 2 | Aluminum | 500 | 10 | 100 | 0.8±0.2 |
| | | 2000 | 60 | 500 | |
| 3 | Aluminum | 500 | 10 | 100 | 1.2±0.2 |
| | | 1000 | 60 | 100 | |
| 4 | Glass | 900 | 65 | 100 | 0.4±0.2 |
| 5 | Glass | 700 | 65 | 100 | 0.8±0.2 |
| 6 | Glass | 500 | 65 | 100 | 1.2±0.2 |

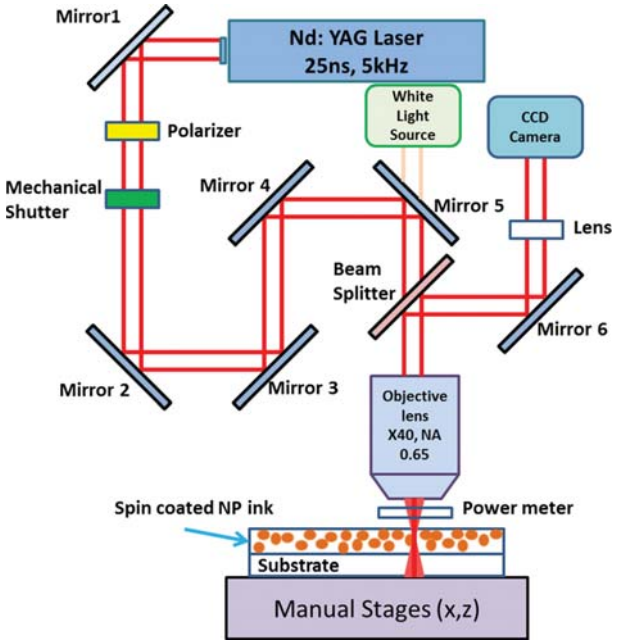


Fig. 25 Schematic of the NS laser sintering setup

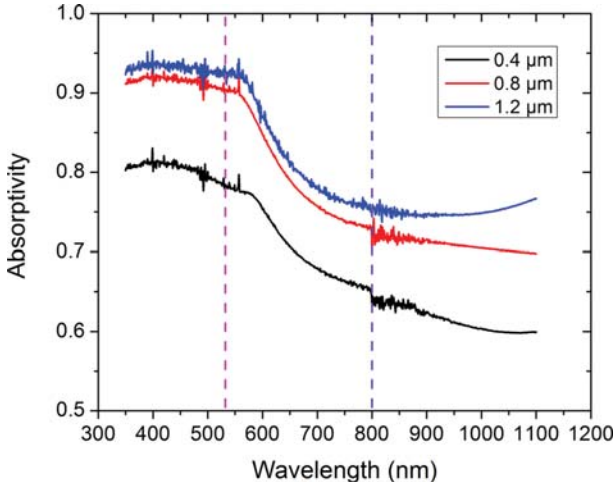


Fig. 26 Absorptivity of Cu ink layer on Al substrate

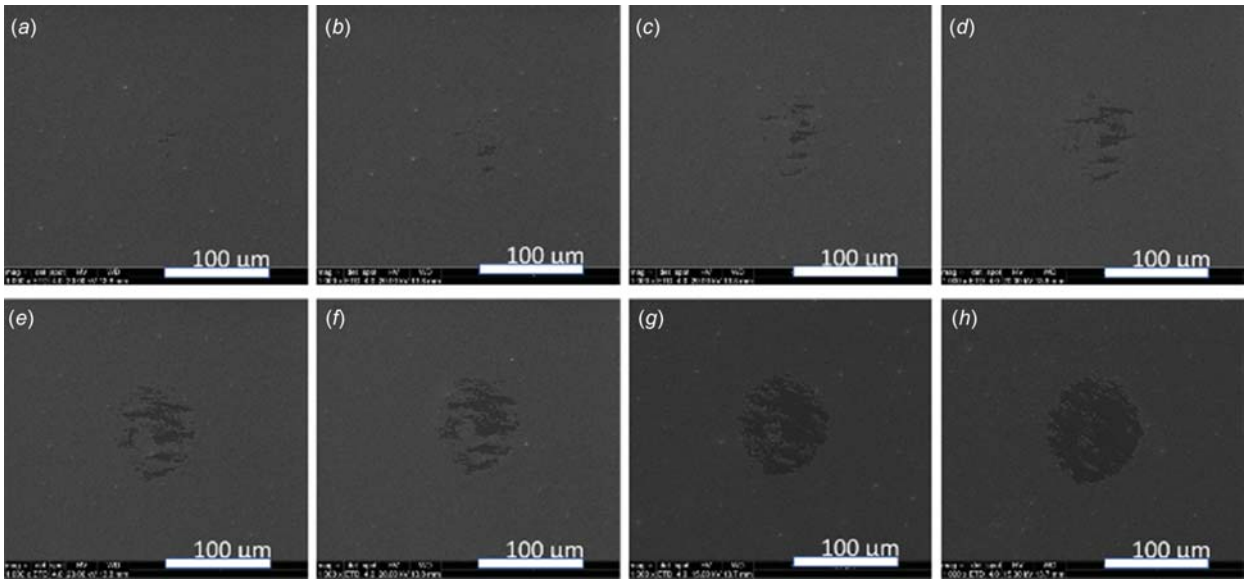


Fig. 27 SEM images of spots sintered using FS laser with (*a*) 9.4±2.3 mJ/cm$^2$, (*b*) 12.6±2.9 mJ/cm$^2$, (*c*) 15.7±3.7 mJ/cm$^2$, (*d*) 18.9±4.3 mJ/cm$^2$, (*e*) 22.1±5.0 mJ/cm$^2$, (*f*) 25.1±5.7 mJ/cm$^2$, (*g*) 37.7±8.4 mJ/cm$^2$, and (*h*) 50.3±11.2 mJ/cm$^2$ for 500 ms on a 0.4 $\mu$m thick Cu layer on Al substrate

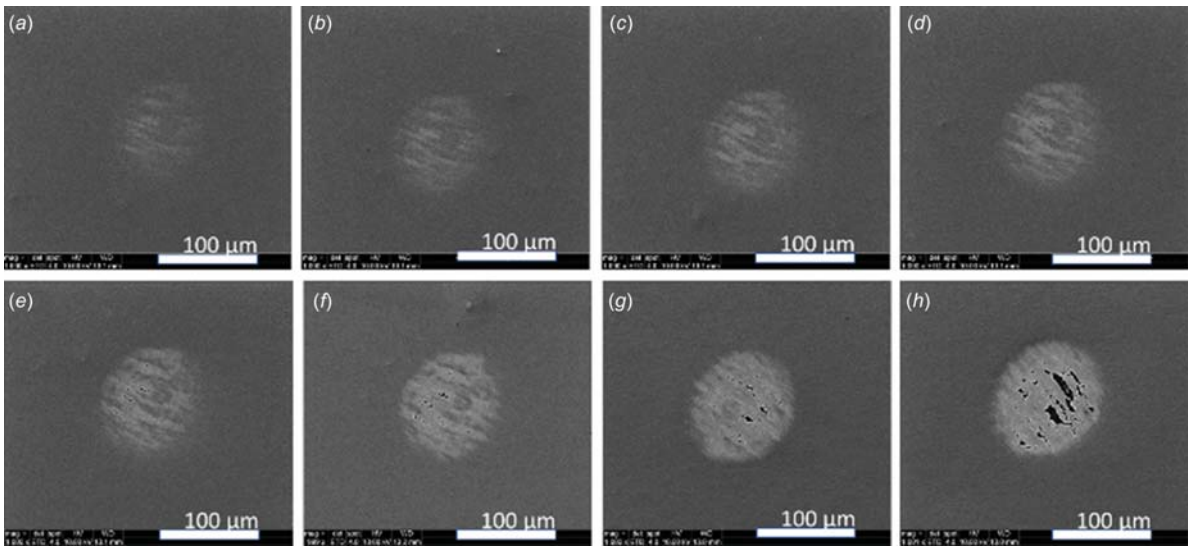


**Fig. 28 SEM images of spots sintered using FS laser with (*a*) 9.4±2.3 mJ/cm$^2$, (*b*) 12.6±2.9 mJ/cm$^2$, (*c*) 15.7±3.7 mJ/cm$^2$, (*d*) 18.9±4.3 mJ/cm$^2$, (*e*) 22.1±5.0 mJ/cm$^2$, (*f*) 25.1±5.7 mJ/cm$^2$, (*g*) 37.7±8.4 mJ/cm$^2$, and (*h*) 50.3±11.2 mJ/cm$^2$ for 500 ms on a 1.2 μm thick Cu layer on Al substrate**

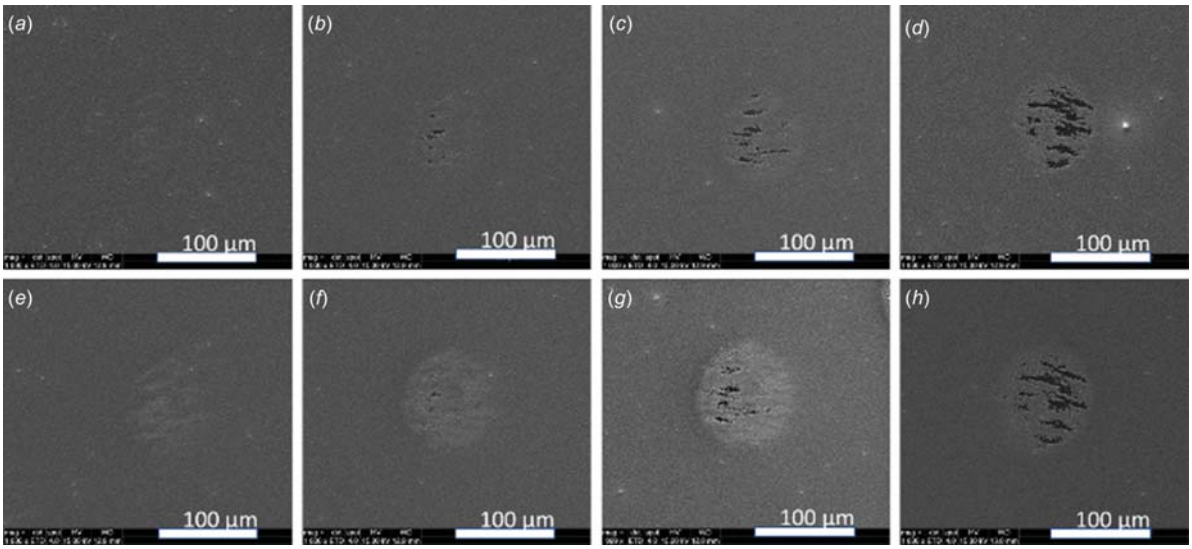


**Fig. 29 SEM images of spots sintered using FS laser with (*a*) 12.6±2.9 mJ/cm$^2$, (*b*) 18.9±4.3 mJ/cm$^2$, (*c*) 25.1±5.7 mJ/cm$^2$, (*d*) 37.7±8.4 mJ/cm$^2$ for 50 ms, (*e*) 12.6±2.9 mJ/cm$^2$, (*f*) 18.9±4.3 mJ/cm$^2$, (*g*) 25.1±5.7 mJ/cm$^2$, and (*h*) 37.7±8.4 mJ/cm$^2$ for 500 ms on a 0.8 μm thick Cu layer on Al substrate**

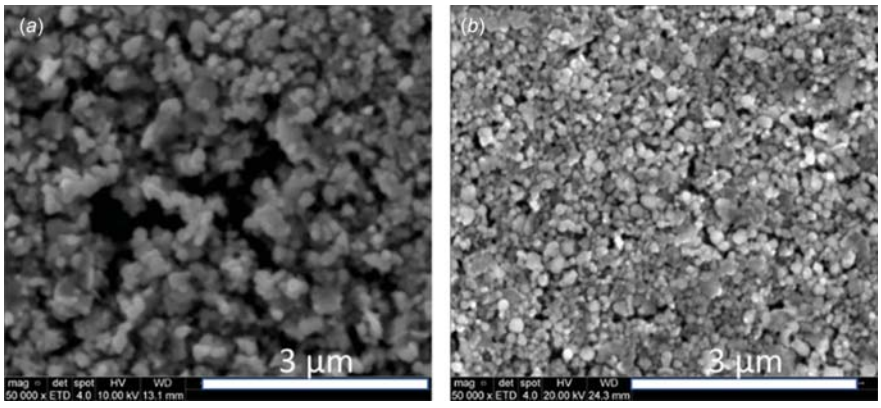


**Fig. 30 Comparison of morphology of FS laser sintered spot with a fluence of (*a*) 15.7±3.7 mJ/cm$^2$ for 50 ms and (*b*) unsintered spots-Al substrate**

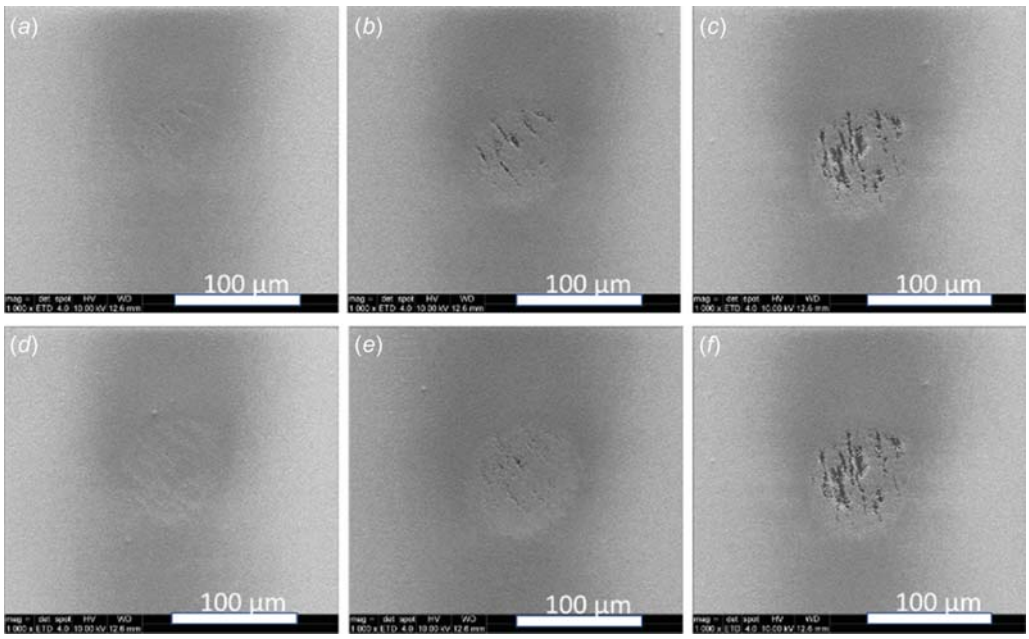


**Fig. 31 SEM images of FS laser sintered spots: (*a*) 18.9±4.3 mJ/cm$^2$, (*b*) 37.7±8.4 mJ/cm$^2$, (*c*) 56.6±12.6 mJ/cm$^2$ for 50 ms and (*d*) 18.9±4.3 mJ/cm$^2$, (*e*) 37.7±8.4 mJ/cm$^2$, and (*f*) 56.6±12.6 mJ/cm$^2$ for 500 ms on 0.8 μm thick Cu layer on glass substrate**

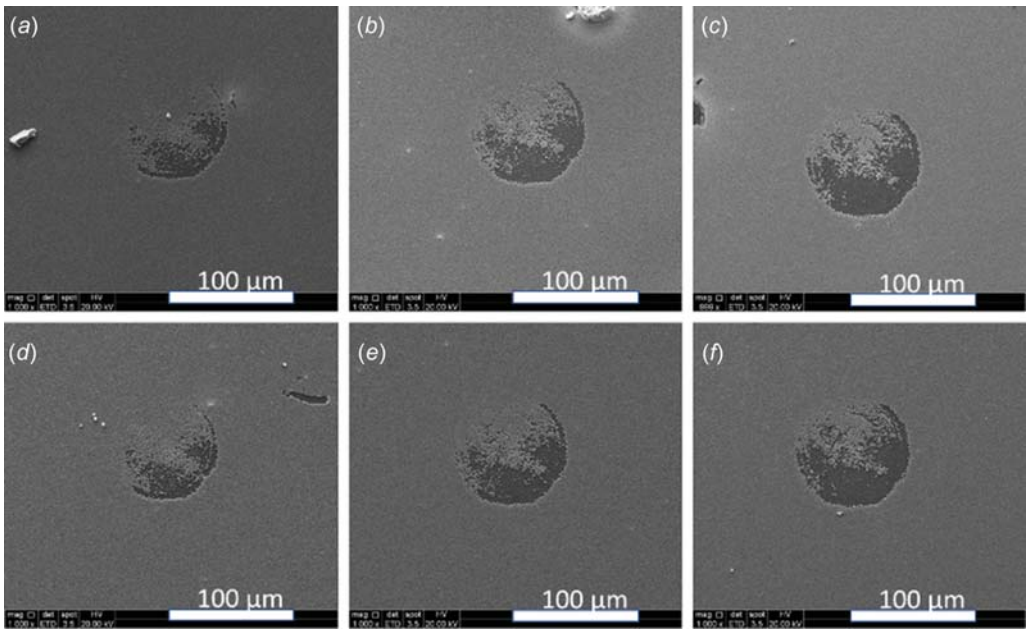


**Fig. 32 SEM images of NS laser sintered spots with (*a*) 152.8±39.8 mJ/cm$^2$, (*b*) 254.6±56.9 mJ/cm$^2$, (*c*) 357.0±75.7 mJ/cm$^2$ for 50 ms, (*d*) 152.8±39.8 mJ/cm$^2$, (*e*) 254.6±56.9 mJ/cm$^2$, and (*f*) 357.0±75.7 mJ/cm$^2$ for 500 ms on 0.8 μm thick Cu layer on Al substrate**

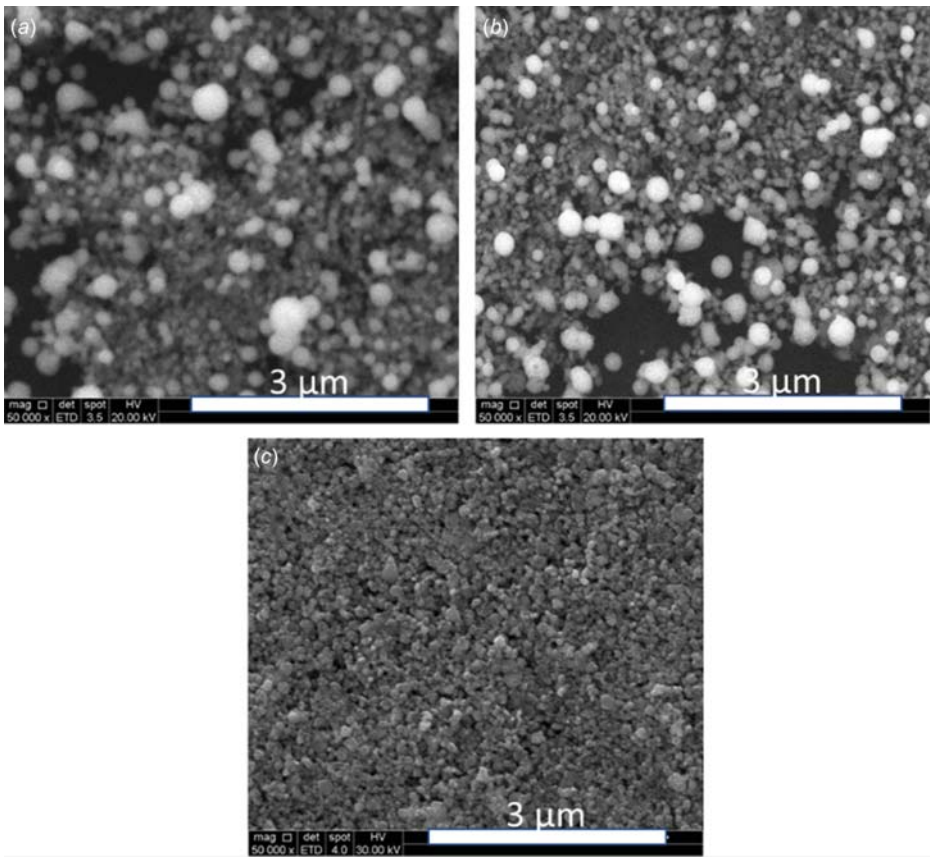


**Fig. 33 Morphology of spots sintered using NS laser with (*a*) 152.8±39.8 mJ/cm$^2$, (*b*) 254.6±56.9 mJ/cm$^2$, and (*c*) unsintered for 50 ms on 1.2 μm thick Cu layer on Al substrate**

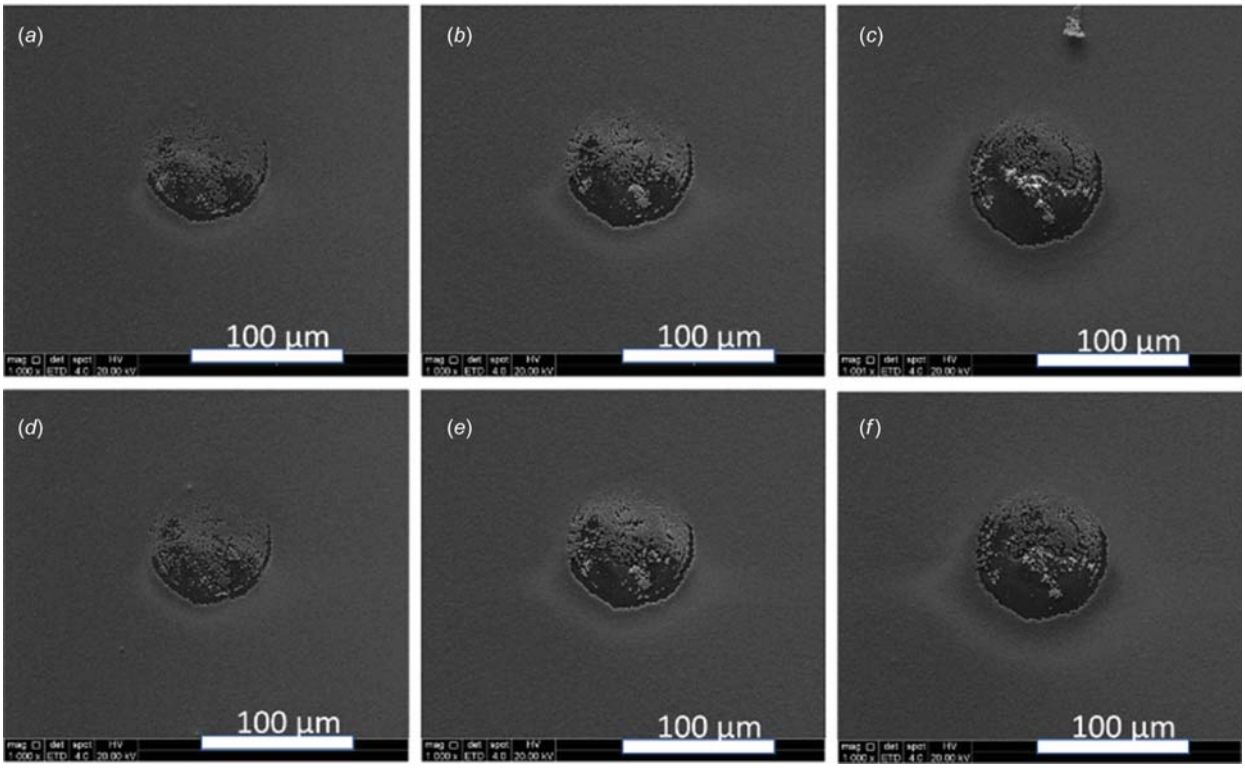


**Fig. 34 SEM images of spots sintered using NS laser with (*a*) 152.8±39.8 mJ/cm$^2$, (*b*) 254.6±56.9 mJ/cm$^2$, (*c*) 357.0±75.7 mJ/cm$^2$ for 50 ms, (*d*) 152.8±39.8 mJ/cm$^2$, (*e*) 254.6±56.9 mJ/cm$^2$, and (*f*) 357.0±75.7 mJ/cm$^2$ for 500 ms on 1.2 μm thick Cu layer on glass substrate**

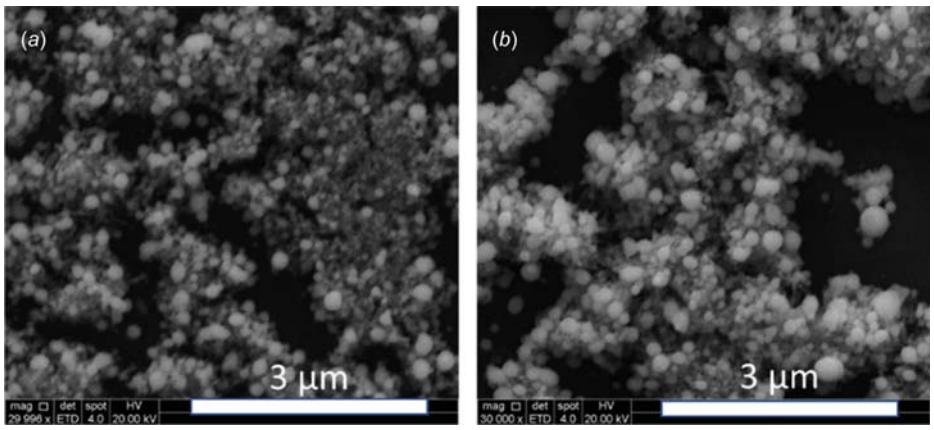


**Fig. 35 Morphology of spots sintered using NS laser with (*a*) 152.8±39.8 mJ/cm$^2$ and (*b*) 254.6±56.9 mJ/cm$^2$ for 500 ms on 1.2 $\mu$m thick Cu layer on glass substrate**

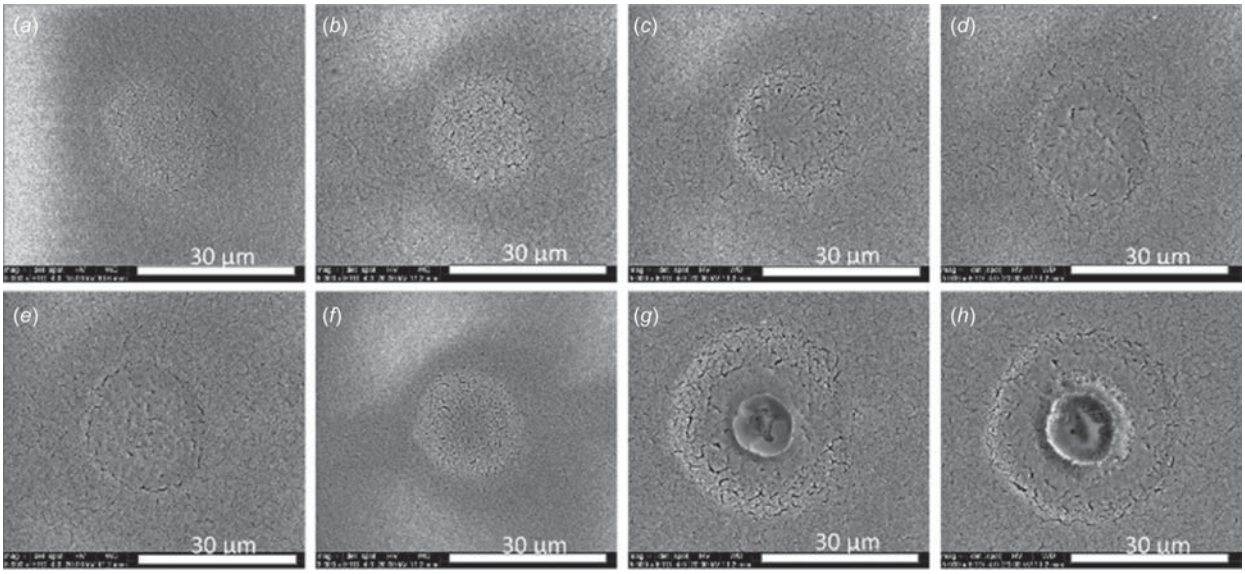


**Fig. 36 SEM images of spots sintered using CW laser with power density 6.5±2.5 kW/cm$^2$ for (*a*) 10 ms, (*b*) 50 ms, (*c*) 200 ms, (*d*) 500 ms and 9.7±3.6 kW/cm$^2$ for (*e*) 10 ms, (*f*) 50 ms, (*g*) 200 ms, and (*h*) 500 ms on 0.8 $\mu$m thick Cu layer on glass substrate**

## Uncertainty Propagation in Fluence Estimates From Model

$$F_{\text{onset necking growth}} = \frac{\rho h C_p (T_f - T_i)}{A}$$

$$\Delta F = \sqrt{\left(\frac{\partial F}{\partial \rho} * \Delta\rho\right)^2 + \left(\frac{\partial F}{\partial h} * \Delta h\right)^2 + \left(\frac{\partial F}{\partial A} * \Delta A\right)^2}$$

$$\frac{\partial F}{\partial \rho} = \frac{h C_p (T_f - T_i)}{A}$$

$$\frac{\partial F}{\partial h} = \frac{\rho C_p (T_f - T_i)}{A}$$

$$\frac{\partial F}{\partial A} = -\frac{\rho h C_p (T_f - T_i)}{A^2} = -\frac{F}{A}$$

$$\Delta\rho = \Delta\left(\frac{\text{mass}}{\text{area} * h}\right) = \sqrt{\left(\frac{\partial \rho}{\partial \text{mass}} * \Delta\text{mass}\right)^2 + \left(\frac{\partial \rho}{\partial h} * \Delta h\right)^2}$$

$$= \sqrt{\left(\frac{\Delta\text{mass}}{\text{area} * h}\right)^2 + \left(-\frac{\text{mass}}{\text{area} * h^2} * \Delta h\right)^2}$$

$$= \sqrt{\left(\frac{\Delta\text{mass}}{\text{area} * h}\right)^2 + \left(-\frac{\rho}{h} * \Delta h\right)^2}$$

$$\Delta A = \Delta(1 - T - R) = \sqrt{\left(\frac{\partial A}{\partial T} * \Delta T\right)^2 + \left(\frac{\partial A}{\partial R} * \Delta R\right)^2}$$

$$= \sqrt{(\Delta T)^2 + (\Delta R)^2}$$

$$T(h) = e^{-\alpha h}$$

$$\Delta T = \frac{\partial T}{\partial h} * \Delta h = -\alpha e^{-\alpha h} * \Delta h = -\alpha T \Delta h$$

$\Delta h =$ error in thickness measurement

$\Delta R =$ error in reflectance measurement

$\Delta \text{mass} =$ error in weight measurement

## References


[1] Mack, C. A., 2011, "Fifty Years of Moore's Law," IEEE Trans. Semicond. Manuf., **24**(2), pp. 202–207.

[2] Roy, N., Dibua, O., Foong, C. S., and Cullinan, M., 2017, "Preliminary Results on the Fabrication of Interconnect Structures Using Microscale Selective Laser Sintering," ASME Paper No. IPACK2017-74173.

[3] Theodorakos, I., Zacharatos, F., Geremia, R., Karnakis, D., and Zergioti, I., 2015, "Selective Laser Sintering of Ag Nanoparticles Ink for Applications in Flexible Electronics," Appl. Surf. Sci., **336**, pp. 157–162.

[4] Yu, X., Mahajan, B. K., Shou, W., and Pan, H., 2016, "Materials, Mechanics, and Patterning Techniques for Elastomer-Based Stretchable Conductors," Micromachines, **8**(1), p. 7.

[5] Roy, N. K., Jou, W., Feng, H., Jeong, J., Wang, Y., and Cullinan, M., 2017, "Laser Sintering of Copper Nanoparticles: A Simplified Model for Fluence Estimation and Validation," ASME Paper No. MSEC2017-2975.

[6] Chen, C. W., and Chen, J. K., 2016, "Femtosecond Laser Sintering of Copper Nanoparticles," Appl. Phys. A, **2016**, pp. 1–8.

[7] Roy, N. K., Foong, C. S., and Cullinan, M. A., 2016, "Design of a Micro-Scale Selective Laser Sintering System," Annual International Solid Freeform Fabrication Symposium (SFF), Austin, TX, Aug. 7–9, pp. 1495–1508.

[8] Roy, N. K., and Cullinan, M. A., 2015, "$\mu$-SLS of Metals: Design of the Powder Spreader, Powder Bed Actuators and Optics for the System," Annual International Solid Freeform Fabrication Symposium (SFF), Austin, TX, Aug. 10–12, pp. 134–155.

[9] Roy, N., Yuksel, A., and Cullinan, M., 2016, "Design and Modeling of a Microscale Selective Laser Sintering System," ASME Paper No. MSEC2016-8569.

[10] Wünscher, S., Abbel, R., Perelaer, J., and Schubert, U. S., 2014, "Progress of Alternative Sintering Approaches of Inkjet-Printed Metal Inks and Their Application for Manufacturing of Flexible Electronic Devices," J. Mater. Chem. C, **2**(48), pp. 10232–10261.

[11] Son, Y., Lim, T. W., Yeo, J., Ko, S. H., and Yang, D.-Y., 2010, "Fabrication of Nanoscale Conductors by Selective Femptosecond Laser Sintering of Metal Nanoparticles," Tenth IEEE International Conference on Nanotechnology (NANO), Seoul, South Korea, Aug. 17–20, pp. 390–393.

[12] An, K., Hong, S., Han, S., Lee, H., Yeo, J., and Ko, S. H., 2014, "Selective Sintering of Metal Nanoparticle Ink for Maskless Fabrication of an Electrode Micropattern Using a Spatially Modulated Laser Beam by a Digital Micromirror Device," ACS Appl. Mater. Interfaces, **6**(4), pp. 2786–2790.

[13] Watanabe, A., 2013, "Laser Sintering of Metal Nanoparticle Film," J. Photopolym. Sci. Technol., **26**(2), pp. 199–205.

[14] Zenou, M., Ermak, O., Saar, A., and Kotler, Z., 2014, "Laser Sintering of Copper Nanoparticles," J. Phys. D: Appl. Phys., **47**(2), p. 25501.

[15] Harzic, R. L., Huot, N., Audouard, E., Jonin, C., Laporte, P., Valette, S., Fraczkiewicz, A., Fortunier, R., Harzic, R. L., Huot, N., Audouard, E., Jonin, C., and Laporte, P., 2016, "Comparison of Heat-Affected Zones Due to Nanosecond and Femtosecond Laser Pulses Using Transmission Electronic Microscopy," Appl. Phys. Lett., **80**(21), pp. 3886–3888.

[16] Ko, S. H., 2014, "Maskless Digital Manufacturing of Organic Thin Film Transistor by Femtosecond Laser Direct Patterning," World Automation Congress (WAC), Waikoloa, HI, Aug. 3–7, pp. 23–26.

[17] Shirk, M. D., and Molian, P. A., 1998, "A Review of Ultrashort Pulsed Laser Ablation of Materials," J. Laser Appl., **10**(1), pp. 18–28.

[18] Gamaly, E. G., Rode, A. V., Luther-Davies, B., and Tikhonchuk, V. T., 2002, "Ablation of Solids by Femtosecond Lasers: Ablation Mechanism and Ablation Thresholds for Metals and Dielectrics," Phys. Plasmas, **9**(3), pp. 949–957.

[19] Kumpulainen, T., Pekkanen, J., Valkama, J., Laakso, J., Tuokko, R., and Mäntysalo, M., 2011, "Low Temperature Nanoparticle Sintering With Continuous Wave and Pulse Lasers," Opt. Laser Technol., **43**(3), pp. 570–576.

[20] Wilson, J., 2007, "Thermal Diffusivity," ITEM Media, Plymouth Meeting, PA, accessed Sept. 15, 2016, https://www.electronics-cooling.com/2007/08/thermal-diffusivity/

[21] Yang, G., Migone, A. D., and Johnson, K. W., 1992, "Heat Capacity and Thermal Diffusivity of a Glass Sample," Phys. Rev. B, **45**(1), pp. 157–160.

[22] Plech, A., Kotaidis, V., Grésillon, S., Dahmen, C., and Von Plessen, G., 2004, "Laser-Induced Heating and Melting of Gold Nanoparticles Studied by Time-Resolved X-Ray Scattering," Phys. Rev. B, **70**(19), p. 195423.

[23] Moon, K.-S., Dong, H., Maric, R., Pothukuchi, S., Hunt, A., Li, Y., and Wong, C. P., 2005, "Thermal Behavior of Silver Nanoparticles for Low-Temperature Interconnect Applications," J. Electron. Mater., **34**(2), pp. 168–175.

[24] Bouguer, P., 1729, "Essai d'optique sur la gradation de la lumière," Charles-Antoine Jombert, Paris, France.

[25] Hultgren, R., Desai, P. D., Hawkins, D. T., Gleiser, M., and Kelley, K. K., 1973, *Selected Values of the Thermodynamic Properties of the Elements*, American Society for Metals, Metals Park, OH, p. 636.

[26] Wolfram Research, 2017, "Heat of Vaporization of the Elements," Wolfram Research, Inc., Champaign, IL, accessed Nov. 1, 2016, http://periodictable.com/Properties/A/VaporizationHeat.an.html

[27] Zhang, Y., Tzou, D. Y., and Chen, J. K., 2015, "Micro-and Nanoscale Heat Transfer in Femtosecond Laser Processing of Metals," e-print arXiv:1511.03566.

[28] Jiang, H., Moon, K., Dong, H., Hua, F., and Wong, C. P., 2006, "Size-Dependent Melting Properties of Tin Nanoparticles," Chem. Phys. Lett., **429**(4), pp. 492–496.

[29] Bachels, T., Güntherodt, H.-J., and Schäfer, R., 2000, "Melting of Isolated Tin Nanoparticles," Phys. Rev. Lett., **85**(6), pp. 1250–1253.

[30] Preuss, S., Demchuk, A., and Stuke, M., 1995, "Sub-Picosecond UV Laser Ablation of Metals," Appl. Phys. A: Mater. Sci. Process., **61**(1), pp. 33–37.

[31] Cabalin, L. M., and Laserna, J. J., 1998, "Experimental Determination of Laser Induced Breakdown Thresholds of Metals Under Nanosecond Q-Switched Laser Operation," Spectrochim. Acta, Part B, **53**(5), pp. 723–730.

[32] Petzoldt, S., Reif, J., and Matthias, E., 1996, "Laser Plasma Threshold of Metals," Appl. Surf. Sci., **96–98**, pp. 199–204.

[33] Piepmeier, E. H., 1986, "Laser Ablation for Atomic Spectroscopy," *Analytical Applications of Lasers*, John Wiley & Sons, New York, pp. 627–669.

[34] Moenke-Blankenburg, L., 1996, "Laser Ablation for Sample Introduction: Principles and Applications," *Laser in Analytical Atomic Spectroscopy*, J. Sneddon, T. L. Thiem, and Y. I. Lee, eds., John Wiley & Sons, Hoboken, NJ, pp. 125–195.

[35] Kaminskienė, Ž., Prosyčevas, I., Stonkutė, J., and Guobienė, A., 2013, "Evaluation of Optical Properties of Ag, Cu, and Co Nanoparticles Synthesized in Organic Medium," Acta Phys. Pol. A, **123**(1), pp. 111–114.

[36] Yeshchenko, O. A., Dmitruk, I. M., Dmytruk, A. M., and Alexeenko, A. A., 2007, "Influence of Annealing Conditions on Size and Optical Properties of Copper Nanoparticles Embedded in Silica Matrix," Mater. Sci. Eng., B, **137**(1), pp. 247–254.

[37] Jeng, M.-S., Yang, R., Song, D., and Chen, G., 2008, "Modeling the Thermal Conductivity and Phonon Transport in Nanoparticle Composites Using Monte Carlo Simulation," ASME J. Heat Transfer, **130**(4), p. 042410.

[38] Kim, W., Zide, J., Gossard, A., Klenov, D., Stemmer, S., Shakouri, A., and Majumdar, A., 2006, "Thermal Conductivity Reduction and Thermoelectric Figure of Merit Increase by Embedding Nanoparticles in Crystalline Semiconductors," Phys. Rev. Lett., **96**(4), p. 45901.

[39] Kruth, J.-P., Mercelis, P., Van Vaerenbergh, J., Froyen, L., and Rombouts, M., 2005, "Binding Mechanisms in Selective Laser Sintering and Selective Laser Melting," Rapid Prototyping J., **11**(1), pp. 26–36.

[40] Casalegno, V., Vavassori, P., Valle, M., Ferraris, M., Salvo, M., and Pintsuk, G., 2010, "Measurement of Thermal Properties of a Ceramic/Metal Joint by Laser Flash Method," J. Nucl. Mater., **407**(2), pp. 83–87.

[41] Chichkov, B. N., Momma, C., Nolte, S., Von Alvensleben, F., and Tünnermann, A., 1996, "Femtosecond, Picosecond and Nanosecond Laser Ablation of Solids," Appl. Phys. A, **63**(2), pp. 109–115.

[42] Farrell, H. H., Petkovic, L. M., Ginosar, D. M., Rollins, H. W., Burch, K. C., and Pinhero, P. J., 2006, "Sublimation Effects in Nanoparticle Catalysts at High Temperatures," ACS National Meeting, San Francisco, CA, Sept. 10–14, Paper No. 1155.

[43] Yim, J. W., Xiang, B., and Wu, J., 2009, "Sublimation of GeTe Nanowires and Evidence of Its Size Effect Studied by In Situ TEM," J. Am. Chem. Soc., **131**(40), pp. 14526–14530.